Large-scale stochastic dynamics of the afterburning in a supersonic fuel-rich plume: possible evidence of unconfined deflagration-to-detonation transition

Stéphane Boulal, Adrien Langenais, Laurent François, Pierre Bernigaud, Lucien Vingert

Large-scale stochastic dynamics of the afterburning in a supersonic fuel-rich plume: possible evidence of unconfined deflagration-to-detonation transition

Stéphane Boulal,[1] Adrien Langenais,[1] Laurent François,[1] Pierre Bernigaud,[1] and Lucien Vingert[1]
DMPE, ONERA, Université Paris Saclay, F-91123, Palaiseau, France

(*Electronic mail: stephane.boulal@onera.fr)

(Dated: 22 January 2025)

The afterburning of a fuel-rich supersonic hot plume exhausting from a model rocket engine exhibited a complex dynamics, whereby the combustion of an unreacted fuel blend – containing hydrogen and carbon monoxide – with atmospheric air neither stabilized nor blew out. High-speed chemiluminescence of the excited hydroxyl radical (OH*) revealed significant stochastic variations of the flame's leading edge location, extending over approximately 25 nozzle diameters in the axial direction. By tracking its apparent motion, we show that the propagation speed of the flame front, relative to the flow, is most of the time well framed by the Chapman-Jouguet (CJ) detonation and deflagration velocities. As such, we infer that the afterburning dynamics consists of an aperiodic cycle of stochastic time-varying phases, including autoignition, deflagration propagation, transition to detonation, detonation propagation, and failure. The mechanism of turbulence-induced spontaneous deflagration-to-detonation transition (DDT) proposed by [A. Poludnenko, T. Gardiner, and E. Oran, Phys. Rev. Lett., 107, (2011)], combined with stationary shock cells at regularly spaced intervals and an overall hot state of the flow, is suspected to be responsible for the repeated initiation of detonations observed in such non-usual unconfined medium. We develop a stochastic model, which is able to reproduce the experimental probability density distribution of the flame's leading edge axial position. Overall, this case study constitutes a challenging benchmark for the validation of Large Eddy Simulation (LES) of scramjet combustors or rocket plumes.

I. INTRODUCTION

Supersonic combustion of partially premixed mixture is paramount for the development of scramjet-based hypersonic propulsion devices[1]. Numerical simulation tools such as Computational Fluid Dynamics (CFD) have the potential to alleviate the development process of supersonic combustors. However, because of the complex physics governing the stabilization of the flame – with phenomena such as autoignition, turbulence-chemistry, shock-flame, and flame-wall interactions, to name a few – relying on the predictions of CFD-based computations is still quite challenging in as much as their predicting capabilities is limited, especially when unsteady combustion is at play.

The non-premixed turbulent burner of Cheng *et al.*[2], which consists of a sonic hydrogen round jet surrounded by a hot Mach 2 vitiated annular air jet, is perhaps the most popular experimental test case, used by various researchers to validate their numerical approaches, because of the large level of instrumentation the experiment was conducted with. Bouheraoua *et al.*[3] provide a recent list of CFD studies, which have aimed at reproducing this experimental case study. Since the flame of Cheng *et al.* stabilizes at a constant lift-off distance of about twenty-five nozzle diameter from the burner exit, its interest is restricted to the study of steady or static – as opposed to dynamic – combustion.

Of course, achieving steady (or stable) combustion is essential when designing a combustion chamber, all the more since this greatly conditions the shape and geometry of the combustor, the wall cooling scheme, *etc.*. Conversely, understanding what causes a flame to be unsteady (or unstable) is equally important, in order to prevent undesired phenomena such as combustion instability, flashback, blowout, or explosions[4,5].

Recently, we conducted an experiment to characterize the afterburning in the supersonic stream of an unreacted fuel blend, containing hydrogen (H_2) and carbon monoxide (CO), as it exhausted into quiescent air from a model rocket engine nozzle. The interest in characterizing this type of configuration is twofold. From a fundamental standpoint, it constitutes a case of supersonic non-premixed combustion, much like the burner of Cheng *et al.*. From a practical viewpoint, afterburning in the exhaust of launchers or missiles greatly influences the heat load they impose on the launch pad, on the afterbody, as well as their radiation signatures[6,7]. The afterburning was predicted to stabilize at a fixed location much like in similar experiments conducted with a Solid Rocket Motor[8] and to a certain extent to the case of Cheng *et al.*. Although the afterburning seems to behave steadily when observed with a regular camcorder of low acquisition-rate and slow shutter speed – as shown in Figure 1 (multimedia available online) – the examination of the afterburning using high-speed chemiluminescence imaging of the hydroxyl radical (OH*) reveals that the flame fails at stabilizing.

FIG. 1. Low acquisition-rate and slow shutter speed imaging of the afterburning, as recorded by a regular camcorder (multimedia available online).

In fact, the afterburning dynamics behaved in a stochastic manner with no apparent regularity and showed excursion of

the flame's leading edge between 3 and 28 nozzle exit diameters. To the best of our knowledge, such large-scale fluctuations have not been reported. Birch and Hargrave[9] studied the flame lift-off height of a supersonic under-expanded natural gas jet mixing and reacting with ambient air. They measured periodic fluctuations covering about 10 nozzle diameters, a magnitude 60% lower than what we experienced. In references[10–12], subsonic non-premixed jet flames featuring normalized fluctuations of their lift-off height spanning up to about 15 nozzle diameters have been reported, which is still 40% lower than the range we experienced. In those experiments, and similarly to ours, the fluctuations were not periodic.

The purpose of this paper is to provide the most complete description of the experiment, which could constitute a challenging validation case for LES-based numerical approaches, turbulent combustion modeling, and chemical kinetic schemes. In Sect. II, we describe the experimental setup. In Sect. III, we provide a thorough description of the observations and basic analysis. In Sect. IV, we describe a non-reactive Reynolds-Averaged Navier–Stokes (RANS) modeling of the jet flow. In Sect. V, we elaborate on the dynamics of the flame's leading edge motion. This is performed by means of a combined use of the experimental observations and the numerical RANS results. In Sect. VI, we discuss the unsteadiness of the afterburning dynamics. Finally, in Sect. VII, we describe a stochastic model, which is able to reproduce the probability density distribution of the flame's leading edge.

II. EXPERIMENTAL SETUP

We conducted the experiment at the MASCOTTE test facility of ONERA with the Bhp-HrM combustion chamber completed at its rear end with an 83-mm-long conical convergent-divergent (CD) nozzle, of throat diameter $d_t = 13.56$ mm and exit diameter $D_e = 27.65$ mm. The nozzle expansion angle is 10.6°. A more complete description of the chamber can be found in[13]. As represented in Figure 2, it consists of a 500-mm-long horizontal duct composed of interchangeable modules of 56 mm diameter circular cross-section. Gaseous methane and oxygen are fed into the combustion chamber through five coaxial injectors (one over the axis of symmetry and the other four positioned symmetrically around it).

The mixture ratio is set to MR ~ 1.8, *i.e.*, in-excess methane is injected with about twice the stoichiometric amount. Combustion within the combustor is thus incomplete leading to a significant unreacted quantity of fuel being transported toward the nozzle exit and subsequently mixed and burnt with the ambient air. The target combustion chamber pressure is $P_c = 2.0$ MPa. In order to protect the throat from the hot gases, a cold film of helium, representing about 9% of the total mass flow rate, is introduced just before the converging section of the nozzle using a circular slit.

Combustion is initiated by a gaseous hydrogen/oxygen torch, which interfaces with the main duct at about a 90° angle immediately downstream of the injector plate. The combustor walls are water-cooled.

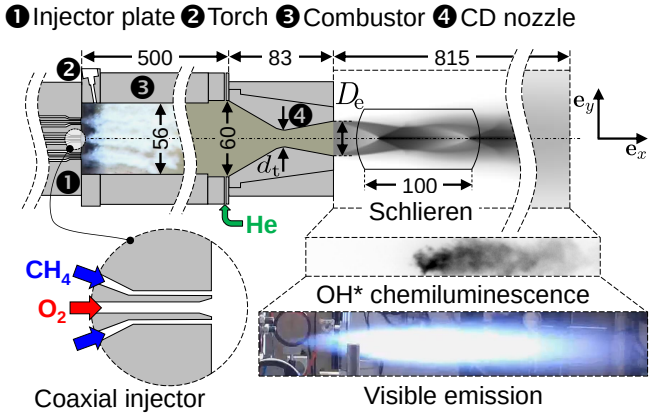

FIG. 2. Overview of the experimental setup used to characterize the afterburning dynamics in the exhaust plume of the model rocket engine. Dimensions are in millimeters. The nozzle throat and exit diameters are $d_t = 13.56$ mm and $D_e = 27.65$ mm. The propellants (methane and oxygen) are injected in the gaseous state.

The supersonic exhaust flow and the afterburning in the plume are characterized by two visualization methods. The first one is a classical in-line Schlieren visualization apparatus set across the supersonic jet. The flow is collimated by means of a Cavilux Smart 400-W pulse laser. It is then focused on a Photron SA3 high-speed camera. We have used a 6.4 kHz recording frequency and the exposure, which in practice is controlled by the laser pulse duration, has been set to 30 ns. The Schlieren setup is horizontally positioned such that the first shock cell is entirely imaged with maximum definition, thus providing the optimal spatial resolution on the camera to validate the RANS computation (see Sect. IV). The second visualization method is the classical OH* chemiluminescence imaging technique, which consists of visualizing the excited hydroxyl radical (OH*) produced by the combustion. This technique is realized using a Phantom V711 high-speed camera coupled with a LaVision HS-IRO image intensifier and a narrowband filter of 310 nm-central wavelength, 10 nm FWHM, and 70% maximum transmission. We have used a 13 kHz recording frequency and a 20 µs gate time for the intensifier. Here, the visualization zone covers about $29.5D_e \approx 815$ mm of the exhaust plume in the axial direction. In order for the two visualization techniques to not interfere with each other, the OH* imaging viewing axis is tilted upward. Hence, we leverage the axisymmetry property of the plume.

III. RESULTS

A. Combustor dynamics

Figure 3 shows the evolutions of the combustion chamber pressure and of the mass flow rates of the different injected constituents. Helium is first injected for about two seconds before the torch valves open and the spark-igniter is triggered – which, for now, sets the time origin $t = 0$ s. About a sec-

TABLE I. Plateau-averaged and rms values of the combustion chamber pressure P_c, mass flow rates $\dot{m}_{(\cdot)}$, and mixture ratio MR $= \dot{m}_{O_2}/\dot{m}_{CH_4}$ for the test case reported in this study.

	P_c (MPa)	$\dot{m}_{O_2}$ (g/s)	$\dot{m}_{CH_4}$ (g/s)	$\dot{m}_{He}$ (g/s)	MR
Average	2.12	113	63	18	1.79
rms	0.012	0.5	0.2	0.1	0.01

ond later, the two propellant valves open. Once the combustion of these in the combustor is confirmed, the torch supply is interrupted ($t = 3$ s). Then, from $t = 5$ s, the reactants and helium mass flow rates throttle up until they reach a stabilized-condition plateau after about ten seconds. This plateau lasts for about fifteen seconds, after which the combustion is quenched by first closing down the oxygen valve ($t = 25.2$ s) and by gradually by-passing the supply source of CH_4 with nitrogen N_2, so as to mitigate the risk of flashback and explosion in the combustor. The average and rms values of the pressure and mass flow rates attained during the stabilized plateau are given in Table I.

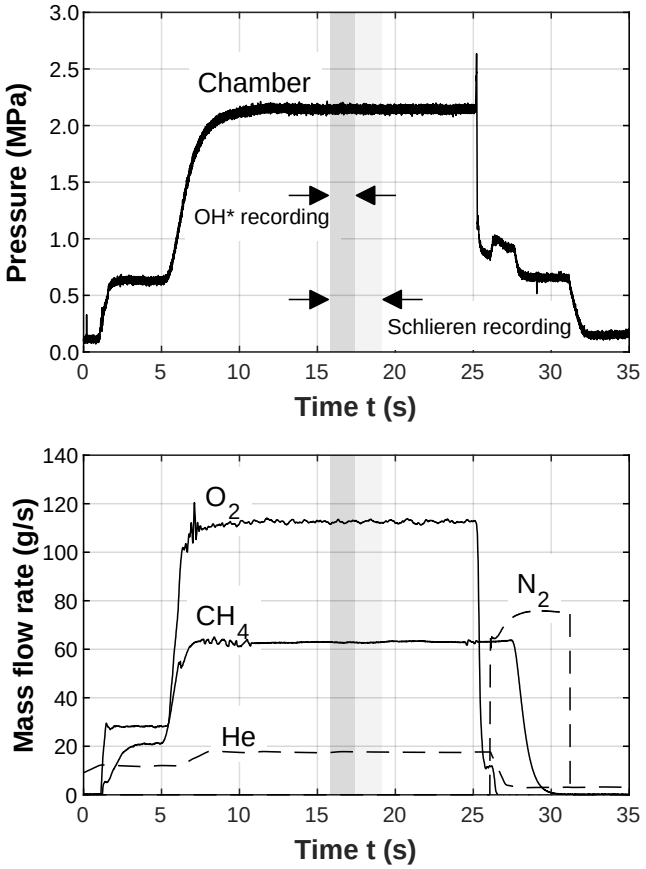

FIG. 3. Evolution of the combustion chamber pressure (top) and mass flow rates (bottom) of the different constituents injected into the combustion chamber (O_2, CH_4, He and N_2 for the purge). The time windows associated with the Schlieren and OH* chemiluminescence high-speed recordings, respectively, are indicated.

Figure 4 shows the spectrogram diagram of the 20 kHz dynamic pressure transducer slightly recessed from the inner wall surface of the combustor. The spectrum contains multiple sharp-frequency peaks at $f \approx 0.4, 0.8, 3.7$ and 9.0 kHz. These are present before ignition and persist even after the combustion is interrupted. They are thus not related to the combustion and constitute noise, which could result from either *(i)* electrical interference captured by the sensor, or *(ii)* vibrations of the bench caused by the water-cooling circuit, since this is operated before, during and after combustion. After ignition and as pressure increases toward the stabilized plateau, we notice the development of a resonance, which signs in the frequency band $1.15 \lesssim f \lesssim 1.35$ kHz, with an rms-based amplitude of 5.8 kPa in that band, representing 50% of the overall rms amplitudes of fluctuation but only 0.27% of the plateau-averaged static pressure. The apparent large peak-to-peak amplitude of the signal, *i.e.*, 0.14 MPa representing $\sim 6\%$ of the plateau-averaged static pressure, mainly comes from the noise discussed above. The theoretical longitudinal acoustic eigenfrequency is $f_{1L} = c/2L$ – with $c \approx 1190$ m/s the average sound speed at equilibrium temperature $T_c = 2034$ K. These values are estimated according to a chemical equilibrium computation using the NASA-CEA code, neglecting the helium contribution (which is only injected in the convergent section) and considering heat loss due to water cooling, modeled as a combustion efficiency of 91%, obtained from water temperature measurements. The characteristic longitudinal dimension L is the distance between the injector plate and the nozzle throat: $L = 0.544$ m, which leads to $f_{1L} = 1.1$ kHz, a value quite close to the excited frequency band of Fig. 4. This suggests that combustion triggers an acoustic resonance of the fundamental longitudinal eigenmode.

This resonance is, however, constrained within the combustor due to the sonic throat. Hence, it has little or no influence on the afterburning dynamics. In fact, the peak frequency of the 1L acoustic eigenmode no longer appears in the spectral analysis of the exhaust plume carried out in §III C.

B. Aerodynamics of the supersonic exhaust plume

Isentropic flow relationships assuming frozen chemistry – with the chemical equilibrium obtained at $P_c = 2.12$ MPa, $T_c = 2034$ K from NASA-CEA and the assumptions given above – allow for the determination of the exit Mach number and static pressure: $M_e = 2.78$ and $P_e = 0.072$ MPa, confirming the initial intention to obtain an overexpanded supersonic flow: the pressure ratio at the nozzle exit is thus $P_e/P_\infty = 0.71$. The exit flow temperature is $T_e = 945$ K. The ideal expanded Mach number is $M_j = 2.60$ and the corresponding ideal exit diameter for perfect expansion at atmospheric pressure would be $D_j = 24.81$ mm. The equilibrium composition of the burnt gases found in the core of the flow (thus excluding helium) evaluated by NASA-CEA is given for reference in Table II. The latter will be used to establish the properties of the main inlet boundary condition in the CFD analysis described in Sect. IV. The unreacted fuel mixture, made up of H_2 and CO, represents 73% in volume and 62% in mass of the exhaust flow. Note that such a gas could be referred to

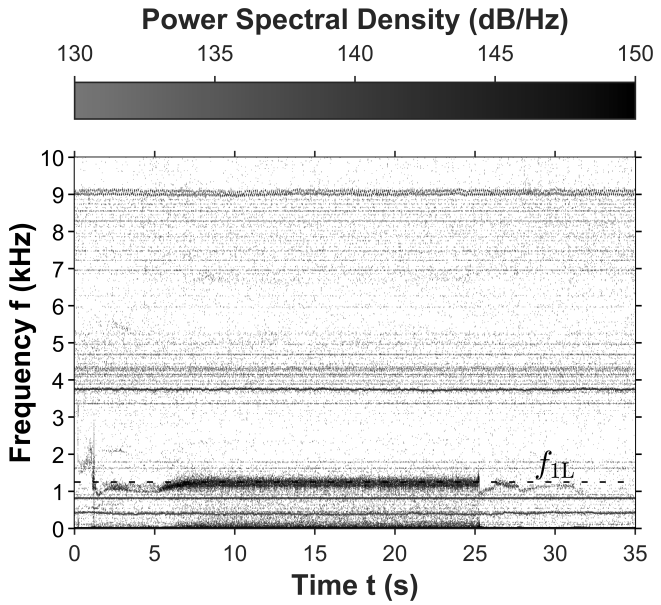

FIG. 4. Spectrogram of the 20-kHz dynamic pressure transducer mounted on the combustor wall.

TABLE II. Mole and mass fractions X_j and Y_j of the most prevailing gaseous species issuing from the nozzle core assuming frozen chemistry and excluding the helium flux.

Species	H_2	CO	H_2O	CO_2
X_j	0.433	0.299	0.234	0.035
Y_j	0.058	0.559	0.281	0.102

as a form of *syngas*. The exit (or jet) Reynolds number is $\mathrm{Re} = 2.3 \times 10^5$, *i.e.*, one order of magnitude larger than in the experiment of Cheng *et al.*[2].

Figure 5(a) shows an instantaneous frame (multimedia available online) of the Schlieren recording and Fig. 5(b) corresponds to the time-averaged image over the stabilized plateau. The compressible features classically observed in such a flow, represented in Figure 6, are barely noticeable in the instantaneous frame.

We only notice the strong density gradient associated with the highly turbulent shear layer ❺, which envelops the periodic shock cell pattern. The latter is even more exacerbated by the presence of the low-density helium injected at the entry of the nozzle convergent. Owing to the time-averaging ($N = 21,167$ frames), which filters out the turbulence structure of the shear layer, the aerodynamic organization of the flow reveals itself: the incident ❶ and the reflected ❷ shocks of the first shock cell are clearly observable. They connect at the normalized position $x_1^S/D_e = 1.29$. The reflected shock bounces into the shear layer ❺ at the normalized position $x_1^T/D_e \approx 2.1$ upon which an expansion fan ❸ emerges. The latter does not appear on the Schlieren time-averaged image because it constitutes a comparatively lower gradient of density than the conical incident and reflected shocks. Although barely noticeable because of the low contrast, we distinguish the coalescence of the compression waves ❹ into a new incident shock ❶. The latter forms a new shock cell, of which the first half, *i.e.*, a reflected shock ❷, incepts at $x_2^S/D_e \approx 3.7$.

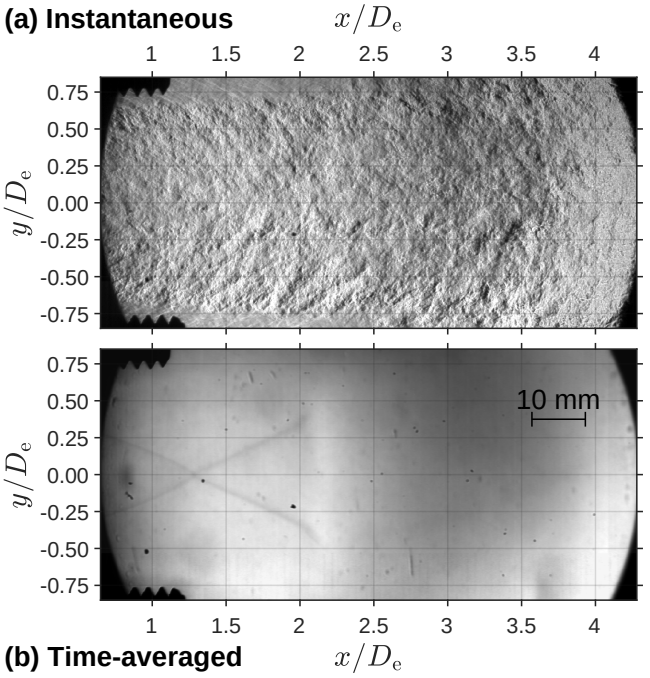

FIG. 5. Schlieren imaging of the supersonic overexpanded jet. **(a)**: Instantaneous 30-ns-long exposure snapshot (multimedia available online). **(b)**: Time-averaged image. The nozzle exit diameter is $D_e = 27.65$ mm.

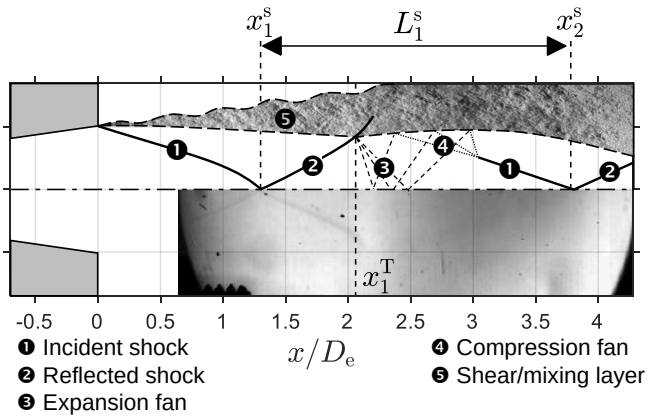

FIG. 6. Aerodynamic structure of the supersonic overexpanded exhaust plume superimposed to the time-averaged Schlieren image.

C. Afterburning dynamics

Figure 7(a) provides a selection of snapshots taken from the $N = 20,448$ frames constitutive of the OH* chemiluminescence recording (low and high display rates multimedia available online). From the time-averaged image of Fig. 7(b), we can make note that restricting the observation of the ex-

haust with too long the exposure, *e.g.*, with a conventional recording of slow shutter speed (see Fig. 1), would incorrectly suggest a spread yet steady afterburning.

The axial position x_f of the flame's leading edge is determined using image binarization with a fixed threshold. Of the $N = 20{,}448$ frames, the leading edge is always observed within the imaged portion of the jet. Figure 8 shows the corresponding time series. The position of the leading edge appears to fluctuate with no apparent regularity.

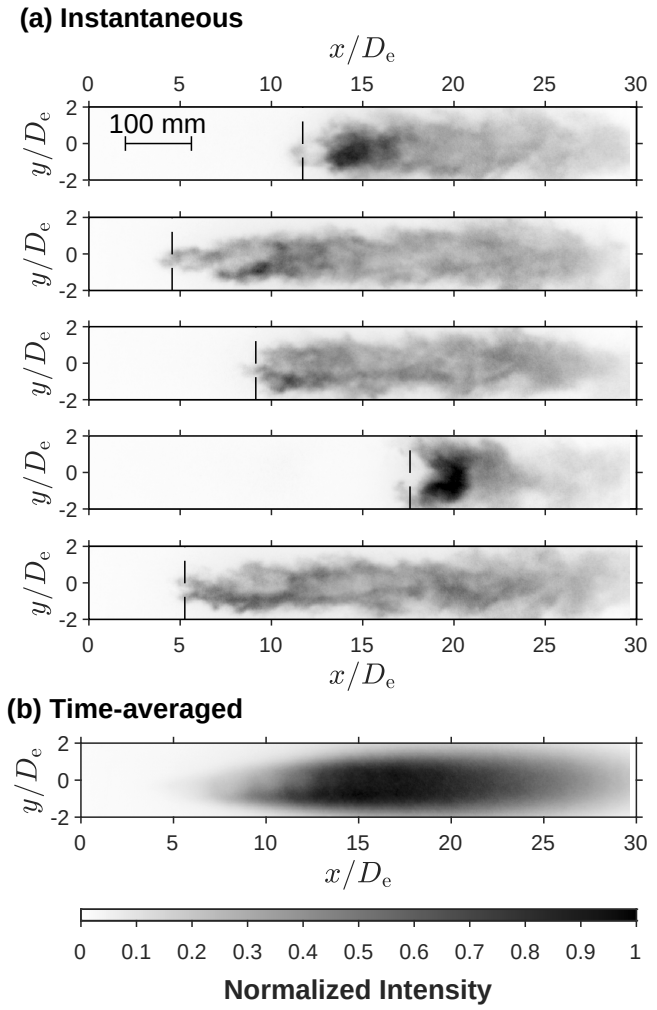

FIG. 7. OH* chemiluminescence imaging of the afterburning dynamics. **(a)** Selection of 20-µs-long exposure snapshots (low and high display rates multimedia available online). The estimated axial position x_f of the flame's leading edge is represented by the vertical dashed line. **(b)** Time-averaged image.

The absence of periodicity is confirmed through a spectral analysis. On the one hand, we perform an FFT of the leading-edge position. On the other hand, we conduct a Spectral Proper Orthogonal Decomposition[5,13,14] of the OH* chemiluminescence recording. The results of the combined spectral analysis is provided in Figure 9. On both spectra, we do not note any unambiguous frequency peaks, which would have suggested a periodical dynamics. Because of the underlying stochastic fluctuations, which appear to be embedded in the

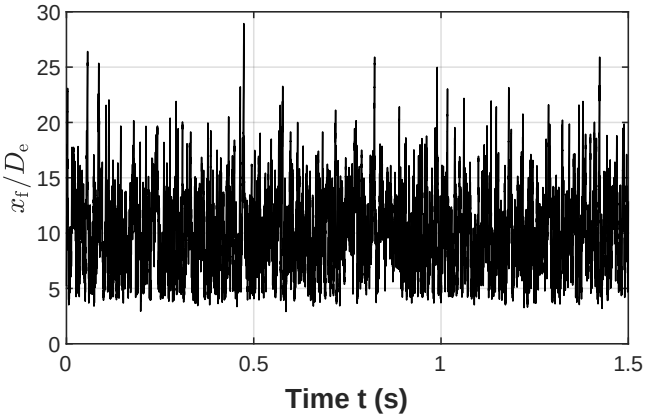

FIG. 8. Time series of the flame's leading edge axial position x_f.

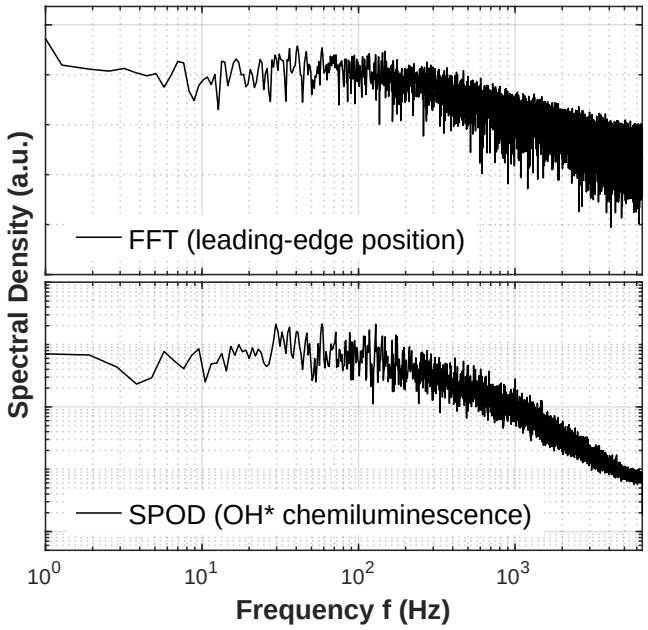

FIG. 9. Top: FFT spectrum of the flame's leading edge axial position x_f (the signal shown in Fig. 8). Bottom: SPOD spectrum (most-dominant modes) of the OH* chemiluminescence recording.

afterburning dynamics, we could only resort to a probabilistic description.

Figure 10 shows the probability density distribution $f(x_\mathrm{f})$ of the flame's leading edge axial position. We verified the statistical convergence of the dataset by drawing randomly half of the dataset multiple times. Each time, we compute the relative error, in the least-square sense, between the obtained distribution and the distribution f, which contains the complete dataset. Over $1{,}000$ draws, the error lies between 3.5 and 9.5%, with a mean error of 5.7%. Thus, the obtained distribution can be considered sufficiently converged.

The distribution appears to be of positive skew and possesses quite a large spread. Afterburning is observed within the range $3 < x/D_\mathrm{e} < 28$. The distribution features local surges, where it jumps from a baseline near log-normal pro-

file. These peaks are found at normalized positions $x/D_e \approx 4.7, 7.1, 9.0, 11.0$ and 12.8. Owing to the non-reactive RANS computation, described in Sect. IV, we find that these positions correspond to locations where the reflected shocks and the shear layer intersect (see Fig. 6). This, in turn, induces jumps in the mixture temperature and drops of the characteristic chemical reaction, or equivalently, surges of the Damköhler number. Physically, these spots act as promoters of flame stabilization in as much as the intersection of the shock with the shear layer creates a reduction of the chemical time scale by increasing the temperature and density of the reactants. They are no longer present in the right tail of the distribution, presumably because the shock-cell structure vanishes as the plume develops. The mechanism of shock-assisted combustion stabilization has been largely suggested in previous numerical works, *e.g.*,[3,15,16], which have attempted to simulate the burner of Cheng *et al.*.

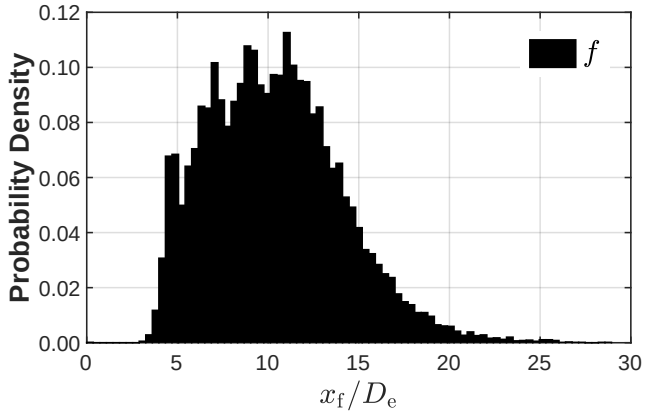

FIG. 10. Probability density distribution f of the flame's leading edge axial position x_f.

IV. NON-REACTIVE RANS COMPUTATION

A 2D-axisymmetric steady RANS computation reproducing the MASCOTTE jet experiment is performed with the aim of providing a numerical flow field as a complementary tool for the analysis of the afterburning behavior. A non-reactive approach is preferred here because the computation of the metrics of interest, such as the local combustion time scale or the flame propagation velocity, only makes sense along unburnt gas streamlines.

A. Numerical models and setup

The computation is conducted following the strategy proposed in Ref.[8], wherein an analogous hot supersonic jet was studied. The axisymmetric compressible RANS equations are solved by means of the multiphysics simulation code CEDRE developed at ONERA. Examples of RANS simulations of supersonic flows achieved with this code can be found in the literature, *e.g.*,[1,7,17,18]. The fluid dynamics solver used here is based on a cell-centered finite-volume method applied to general unstructured elements[19]. The specific heats of transported species are approximated by polynomials of 7th order. The viscosity of species is determined according to the Sutherland law. The time integration is carried out with an implicit 1st order scheme, whereas the space discretization is of 2nd order, the convective fluxes being computed with a Harten-Lax-van Leer-Contact scheme.

TABLE III. Values of the shock cell structure metrics.

	Experiment	Non-reactive RANS
x_1^S/D_e	1.29	1.29
x_2^S/D_e	3.7	3.77
x_1^T/D_e	2.1	2.0

Turbulence is modeled by a two-equation k-ω approach assuming a classical Boussinesq hypothesis, where the turbulent scalars k and ω are, respectively, the turbulent kinetic energy and the specific turbulence dissipation rate. We adopt the Shear-Stress Transport (SST) formulation of Menter *et al.*[20] with a source term based on vorticity[21] to avoid non-physical production of turbulence through shocks. Both Pope and Sarkar corrections are implemented to handle the round-jet/plane-jet anomaly[22] as well as compressibility effects[23].

The numerical domain includes the convergent-divergent nozzle and the associated external walls represented in Fig. 2. It extends downstream over $145\,D_e$ in the axial direction and $72.5\,D_e$ in the radial direction. A mesh composed of 1.35×10^6 unstructured elements is generated, with layers of quad cells in the nozzle wall. In order to ensure grid convergence, the cell sizes are set smaller than those employed in[8] for the selected mesh. The combustion chamber conditions are prescribed at the convergent inlet boundary as those obtained from the equilibrium state given in §III B, *i.e.*, $P_c = 21.2\,\mathrm{MPa}$, $T_c = 2034\,\mathrm{K}$ and the mass fractions of Tab. II. Helium is also introduced in the vicinity of the convergent wall to take the film-cooling into account. Boundaries at the ambient air condition – $P_\infty = 0.1\,\mathrm{MPa}$ and $T_\infty = 285\,\mathrm{K}$ – are set elsewhere. The exit pressure $P_e = 0.075\,\mathrm{MPa}$, temperature $T_e = 960\,\mathrm{K}$ and Mach number $\mathrm{M}_e = 2.76$, close to the theoretical isentropic values, are recovered in the exit plane of the nozzle. The corresponding jet exit velocity is $u_e = 2300\,\mathrm{m/s}$.

Figure 11 compares the mean density gradient magnitude to the time-averaged Schlieren image. The first shock locations on the jet axis and in the mixing layer, reported in Tab. III, agree well with the experiment. Figure 12 shows the mean axial velocity and temperature fields. In the region $3 < x/D_e < 28$ of interest for the dynamics of the afterburning, the temperature generally spans the range $800 - 1200\,\mathrm{K}$ and the velocity covers the range $500 - 2000\,\mathrm{m/s}$. The lengths of the jet potential core ($u_x < 0.95u_e$) and supersonic region can be deduced from these fields: $L_{core} = 10\,D_e$ and $L_{sonic} = 21\,D_e$.

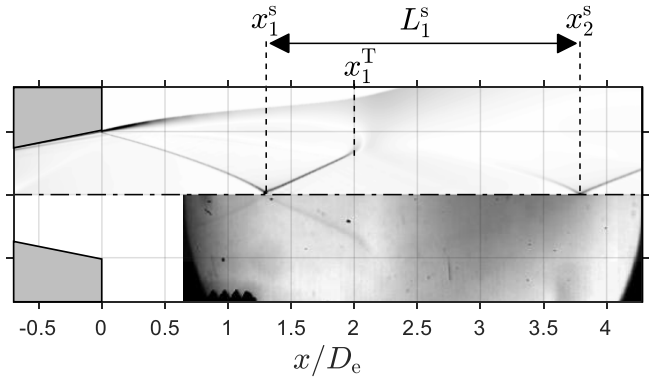

FIG. 11. Comparison of the mean density gradient magnitude field from the 2D-axisymmetric RANS computation (top) to the time-averaged Schlieren image (bottom).

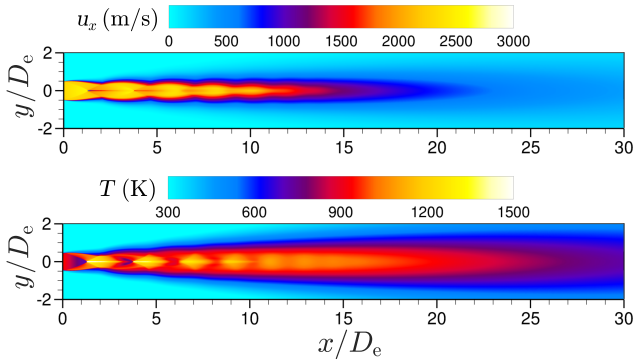

FIG. 12. Average axial velocity u_x (top) and temperature T (bottom) fields obtained from the 2D-axisymmetric RANS computation.

B. Post-computation of the turbulent combustion characteristic time scales

The numerical flow solution is used to evaluate the local turbulent Damköhler number, defined as the ratio of characteristics turbulence and chemistry time scales, providing a measure of the competition between combustion and turbulence:

$$\mathrm{Da} = \frac{\tau_\mathrm{t}}{\tau_\mathrm{c}} \tag{1}$$

where the turbulent time scale τ_t is deduced from ω as $\tau_\mathrm{t} = 1/(\beta^*\omega)$, with $\beta^* = 0.09$ a constant of the SST model recommended by Menter[20]. This time scale relates to the integral length scale ℓ_t. The chemical time scale τ_c is post-computed using zero-dimensional constant-pressure CHEMKIN reactors and the chemical kinetic scheme proposed by Troyes *et al.*[8,17] fed by the composition, temperature, and pressure conditions extracted from the flow solution. We limit the post-computation region to the mixture fraction range $0.05 < Z < 0.95$, where Z is equal to unity in the jet core and zero in the ambient air (see[8] for the definition of Z). In practice, the time scale τ_c is defined as the time at which the maximum of the temperature variation rate $\mathrm{d}T/\mathrm{d}t$ is reached. The resulting fields of τ_c and Da are shown in Figure 13. Minimum chemical time scale values on the order of $\tau_\mathrm{c} \simeq 8\times10^{-5}\,\mathrm{s}$ are found immediately downstream of the reflected shocks intersecting the mixing layer, similar to the peaks observed in Fig. 10. These also correspond to the locations of the Damköhler-number surges. However, the maximum value of Da, just above unity, is reached past the end of the potential core, at $x/D_\mathrm{e} = 19.5$, which corresponds to a region where the turbulent time scale of the flow significantly increases.

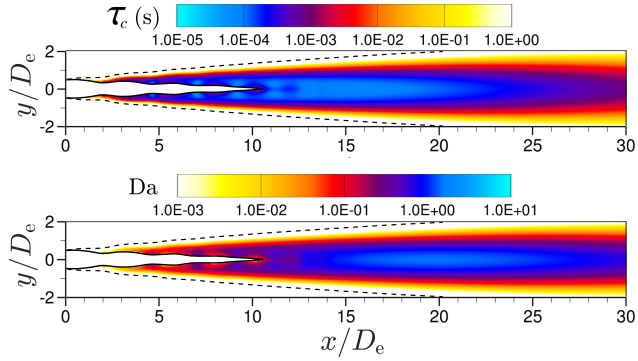

FIG. 13. Chemical time scale τ_c in the mixing layer region $0.05 < Z < 0.95$ obtained from constant-pressure CHEMKIN reactor computations (top) and the corresponding field of the turbulent Damköhler number Da (bottom). Dashed black line: $Z = 0.05$ iso-line; Solid black line: $Z = 0.95$ iso-line.

V. ANALYSIS

The variation of the flame's leading edge position from $x_\mathrm{f}(t_k) = x_\mathrm{f}^k$ to $x_\mathrm{f}(t_{k+1}) = x_\mathrm{f}^{k+1}$ in between two frames, *i.e.*, over one time step $\Delta t = t_{k+1} - t_k \approx 77\,\mu\mathrm{s}$, either results from *(i)* the spontaneous creation of a combustion kernel, *i.e.*, an autoignition if $x_\mathrm{f}^{k+1} < x_\mathrm{f}^k$, *(ii)* the convection of an autoignition spot with a velocity close to u_x if $x_\mathrm{f}^{k+1} > x_\mathrm{f}^k$, or *(iii)* the continuous propagation of a combustion front. In cases *(i)* and *(ii)*, the displacement of the leading edge would only be an apparent motion. In case *(iii)*, the displacement of the leading edge would be that of a reactive front. To examine this point, we propose to determine the speed s_f such a front would have.

Figure 14 provides a visual summary of the assumptions utilized in evaluating the front speed. Let us first assume that the front propagates as a premixed front. Since the flame does not attach to the nozzle lip, there should exist a finite volume constrained in the mixing layer (the shaded area in Fig. 6), within which this hypothesis holds.

The composition of velocity[24] between the apparent displacement velocity $d\mathbf{X}_\mathrm{f}/dt$ of the front, the (intrinsic) front speed s_f, and the local velocity of the flow $\mathbf{u}$ writes:

$$\frac{d\mathbf{X}_\mathrm{f}}{dt} \triangleq \mathbf{u} + \mathbf{n}\cdot s_\mathrm{f} \tag{2}$$

where $\mathbf{n}$ is a unit normal vector directed toward the unburnt gases. The flow and propagation of the leading edge are essentially one-dimensional, *i.e.*, $\mathbf{u} \approx u_x\mathbf{e}_x$ and $d\mathbf{X}_\mathrm{f}/dt \approx$

$(dx_\mathrm{f}/dt)\,\mathbf{e}_x$, where $\mathbf{e}_x$ is the x-direction vector of the standard basis. In a first approach, we therefore consider that the front propagates only in the x-direction, that is, $\mathbf{n} = n_x\mathbf{e}_x = -\mathbf{e}_x$. The velocity composition is arranged such that:

$$\frac{dx_\mathrm{f}}{dt} \approx u_x - s_\mathrm{f} \tag{3}$$

in such a way that a negative displacement, *i.e.*, $dx_\mathrm{f} < 0$, corresponds to $s_\mathrm{f} > u_x$, whereas a positive displacement, *i.e.*, $dx_\mathrm{f} > 0$, suggests $s_\mathrm{f} < u_x$. Equation (3) is re-written into the form:

$$s_\mathrm{f} \approx u_x - \frac{dx_\mathrm{f}}{dt} \tag{4}$$

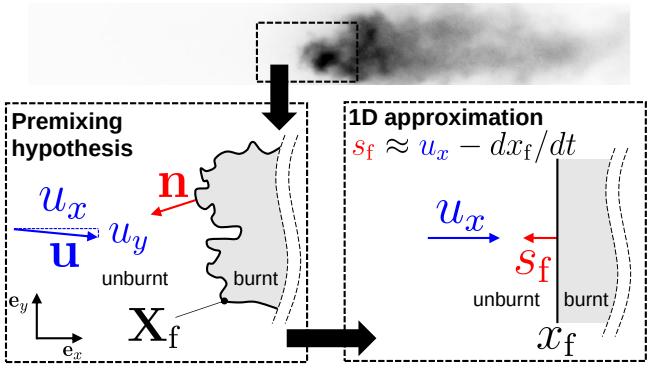

FIG. 14. Schematic illustration of the methodology and assumptions considered to evaluate the flame front speed s_f from the apparent displacement velocity dx_f/dt of the flame's leading edge and axial flow velocity u_x.

Since the flow speed u_x is not measured, we approximate its value by a specific averaging of the velocity field obtained in the RANS simulation. Considering that the flame front is likely to propagate in the vicinity of the streamline of maximum reactivity, identified at each cross-section by the maximum of the Damköhler number, we find it convenient to introduce a weight-averaging operator, noted $\widetilde{\cdot}$, which, for any variable g, returns the value $\widetilde{g}$:

$$\widetilde{g}(x) \triangleq \frac{\int_y \mathrm{Da}(x,y)g(x,y)\,\mathrm{d}y}{\int_y \mathrm{Da}(x,y)\,\mathrm{d}y} \tag{5}$$

where $\mathrm{Da}(x,y)$ represents the two-dimensional Damköhler field determined from the RANS non-reactive simulation (see Fig. 13). This operator allows for the evaluation of a one-dimensional average along the radial direction for each variable, favoring values from zones of higher reactivity. We use this procedure to evaluate one-dimensional averages of all the CFD flow field variables. Figures 15 and 16 show the axial profiles of $\widetilde{\mathrm{Da}}$ and $\widetilde{u_x}$ after the weight-averaging operation. Note that different weightings have been tested, *e.g.*, Da^2, or simply using $\widetilde{g}(x) = g(x, \underset{y}{\mathrm{argmax}}\ \mathrm{Da}(x,y))$. They all produced relatively similar profiles, without affecting the results presented later in this paper. Finally, the front velocity s_f is evaluated as:

$$s_\mathrm{f}^{k+1} = \overline{u_x} - \left.\frac{dx_\mathrm{f}}{dt}\right|_{k+1} = \frac{\int_{x_\mathrm{f}^k}^{x_\mathrm{f}^{k+1}} \widetilde{u_x}\,\mathrm{d}x}{\left|x_\mathrm{f}^{k+1} - x_\mathrm{f}^k\right|} - \frac{x_\mathrm{f}^{k+1} - x_\mathrm{f}^k}{\Delta t} \tag{6}$$

It could be argued that the flame could perturb the flow upstream of the front. However, we checked the velocity $\widetilde{u_x} - \widetilde{a_\mathrm{f}}$ of retropropagating acoustic waves is always positive for $x/D_e < 19$, *i.e.*, the flow is supersonic in the region where the flame front propagates (see Fig. 10) and no perturbation can travel upstream.

Naturally, s_f could be ill-estimated because of the 1D approximation considered for the front propagation. Indeed, the flame front could have a 3D trajectory, *e.g.*, following that of a helix, and consequently have the azimuthal and/or radial components of its velocity vector negated. We further examine the consequences of such an approximation later in this section.

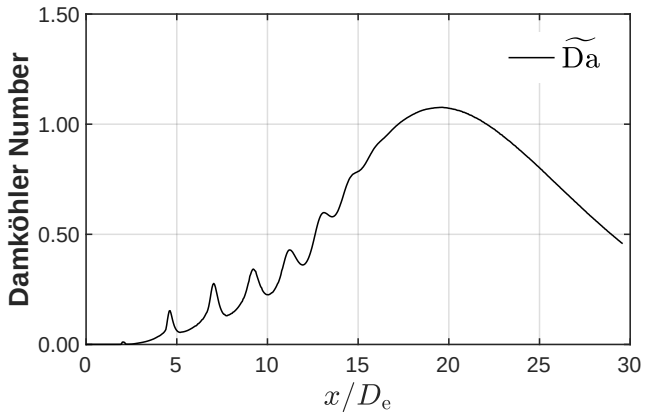

FIG. 15. Profile of $\widetilde{\mathrm{Da}}$ along which the flame front allegedly propagates.

Figure 17 gives the probability density distributions of dx_f/dt measured through the tracking of the flame's leading edge and s_f evaluated by means of Eq. (6). The most frequent displacement velocity is $dx_\mathrm{f}/dt \approx 190$ m/s. Statistically, the leading edge progresses toward upstream locations ($dx_\mathrm{f} < 0$) 38% of the time and toward downstream locations ($dx_\mathrm{f} > 0$) 62% of the time. The most frequent front speed is about $s_\mathrm{f} = 900$ m/s. Figure 18 shows the joint probability density distribution of the front position and speed $(x_\mathrm{f}, s_\mathrm{f})$.

Since $s_\mathrm{f} = 0$ is never observed, we can immediately rule out the possibility that the downstream displacements of the flame's leading edge result from autoignition spots being convected at the flow velocity. This implies that continuous propagations of reactive fronts must counteract the convection. As for the upstream displacements, it will later be shown that they are more likely caused by the continuous propagations of reactive fronts rather than by discontinuous upstream autoignitions.

In order to precise the nature of the reactive fronts, we propose to evaluate the velocity magnitudes of two canonical regimes of flame propagation: the Chapman-Jouguet (CJ)

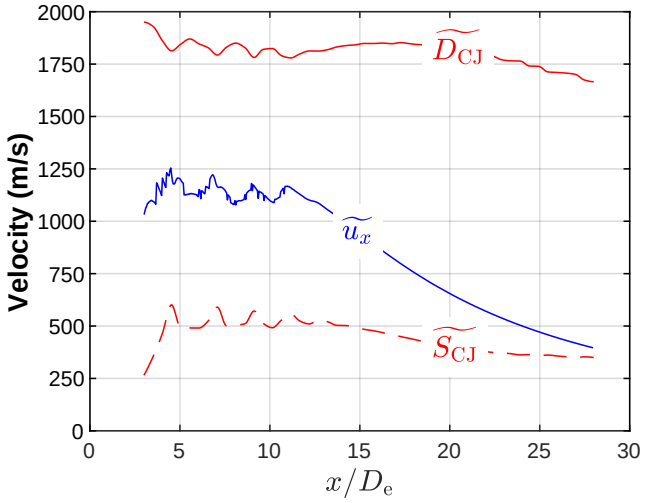

FIG. 16. Profiles of the axial flow velocity $\widetilde{u_x}$ and Chapman-Jouguet deflagration and detonation velocities, $\widetilde{S_{\mathrm{CJ}}}$ and $\widetilde{D_{\mathrm{CJ}}}$, along which the flame front allegedly propagates and for positions visited by the leading edge, *i.e.*, for $3 < x/D_{\mathrm{e}} < 28$.

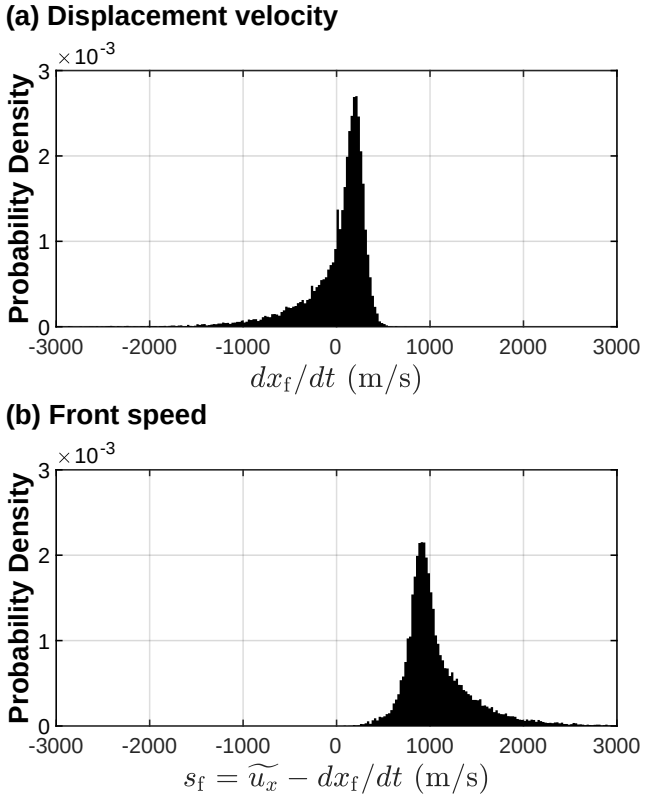

FIG. 17. Probability density distributions of **(a)** the apparent displacement velocity dx_{f}/dt of the flame's leading edge position determined from the OH* chemiluminescence recording and **(b)** the corresponding front speed s_{f} deduced from the local axial velocity $\widetilde{u_x}$ (see Fig. 16).

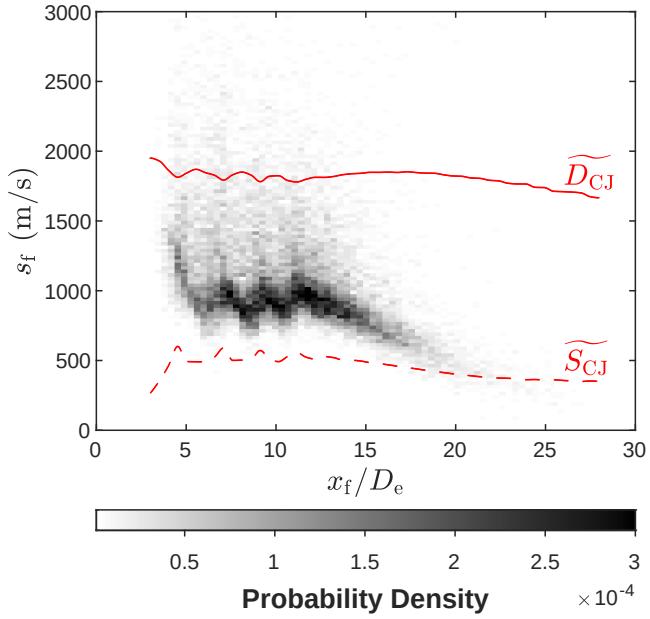

FIG. 18. Joint probability density distribution of the flame's leading edge position x_{f} and corresponding front speed s_{f}.

detonation and deflagration regimes. On the one hand, the CJ detonation regime relates to the propagation of a self-propagating coupled shock/flame complex whereby the flame and the shock front are intimately coupled and support each other. The theoretical detonation velocity D_{CJ} is known for its accuracy in predicting the speeds of non-marginal, multicellular detonation fronts. On the other hand, the CJ deflagration regime[25] usually refers to the regime temporarily attained by the reactive front before the onset of the detonation according to the deflagration-to-detonation transition (DDT) phenomenology. It was also suggested[26] that this is the regime attained when a detonation fails into a decoupled shock-flame complex. According to[27], the CJ deflagration velocity is the largest speed achievable by a steady propagating flame without a shock. In terms of terminology, we can distinguish two subcategories of deflagration regimes: the *slow* deflagration regime, which corresponds to front speeds $s_{\mathrm{f}} < S_{\mathrm{CJ}}$ and the *choked* deflagration regime, which corresponds to front speeds $s_{\mathrm{f}} > S_{\mathrm{CJ}}$[28]. The latter is inherently unstable since its shock-flame complex is attracted toward DDT. According to Poludnenko *et al.*[29], in unconfined medium, S_{CJ} could be approximated to $S_{\mathrm{CJ}} = a_{\mathrm{b}}/\alpha$, where a_{b} is the sound speed in the burnt gases of an isobaric combustion, and α is the density ratio across the flame: $\alpha = \rho_{\mathrm{f}}/\rho_{\mathrm{b}}$ (f: fresh reactants, b: burnt gases).

Using NASA-CEA, we compute the local CJ detonation and deflagration velocities, $\widetilde{D_{\mathrm{CJ}}}$ and $\widetilde{S_{\mathrm{CJ}}}$, considering mixtures of which the composition, temperature and pressure are weight-averaged from the RANS field at each cross-section, according to Eq. (5), and for positions visited by the flame's leading edge, *i.e.*, for $3 < x/D_{\mathrm{e}} < 28$. Figures 16 and 18 display the profile of $\widetilde{S_{\mathrm{CJ}}}$ and $\widetilde{D_{\mathrm{CJ}}}$, hence evaluated. It can be observed that the front speed s_{f} is well-framed by the two limits, that is $\widetilde{S_{\mathrm{CJ}}} \lesssim s_{\mathrm{f}} \lesssim \widetilde{D_{\mathrm{CJ}}}$, for about 95% of the statistical sample. The flame speed appears therefore to fluctuate be-

tween the regimes of choked deflagrations ($s_f \gtrsim \widetilde{S_{CJ}}$) and detonations ($s_f \lesssim \widetilde{D_{CJ}}$). To some extent, this resembles the quasi-detonation regime observed in obstructed channels[25,30]. The most observed velocity is $s_f = 900$ m/s $\approx 1.8\widetilde{S_{CJ}} \approx 0.5\widetilde{D_{CJ}}$. The slow deflagration regime, *i.e*, $s_f \lesssim \widetilde{S_{CJ}}$, is not observed. We note some traces of $s_f \gtrsim \widetilde{D_{CJ}}$, which should correspond to the overdriven detonation regime. This highly transient regime is usually observed following the onset of the detonation upon either DDT[31], or direct detonation initiation, such that triggered by the explosion of a spherical high energy point source[31], or when a failed detonation re-initiates[32].

As mentioned earlier, since the OH* chemiluminescence is line-of-sight integrated, the 1D approximation considered for the displacement of the flame's leading edge underestimates the velocity magnitude $|d\mathbf{X}_f/dt|$ of the actual 3D flame motion. Consequently, according to Eq. (4), the approximation $|d\mathbf{X}_f/dt| \approx |dx_f/dt|$ yields an underestimation of s_f if $dx_f/dt < 0$ ($s_f > u_x$) but an overestimation of s_f if $dx_f/dt > 0$ ($s_f < u_x$). On the joint probability density distribution of (x_f, s_f) of Fig. 18, this effect would qualitatively translate into points such that $s_f > u_x$ to move upward and points such that $s_f < u_x$ to move downward. Overall, the cloud of point could then be even more closely bounded by the boundary of $\widetilde{D_{CJ}}$ and $\widetilde{S_{CJ}}$.

Note that the graphs shown in Figs. 17 and 18 are inherently biased toward the lower velocities of the choked deflagration regime. More quantitatively speaking, let us consider the region $4 \lesssim x/D_e \lesssim 15$, where detonation-like velocities are observed. Here, the flow velocity is about $\widetilde{u_x} \approx 1100$ m/s. Considering that the characteristic front speeds of a detonation and a deflagration (choked regime) are, respectively, $s_f = \widetilde{D_{CJ}} \approx 1800$ m/s and $s_f \approx 900$ m/s, the former progresses upstream with an apparent velocity $dx_f/dt \approx u_x - s_f \approx -700$ m/s, while the latter progresses downstream with an apparent velocity $dx_f/dt \approx +200$ m/s. To illustrate the idea, let us now consider that during the time period considered, neither fronts experience a transition. From this order of magnitude analysis, we then deduce that the propagation of the deflagration front will be recorded approximately three times more often than that of the detonation front.

Figure 19 shows an example of a possible sequence of deflagration acceleration, detonation propagation, and failure. Figure 20 shows the evolution of the (apparent) displacement velocity dx_f/dt of the leading edge measured during this sequence. The flow axial velocity $\widetilde{u_x}$ evaluated from the RANS computation at the positions x_f visited by the leading edge is also provided. Besides, Fig. 20 shows the corresponding evolution of the front speed s_f evaluated by means of Eq. (6). We observe that the front speed is well framed by the CJ deflagration and detonation velocities. Between the fourth and fifth frames of Fig. 19, *i.e.*, for $t - t_0 \approx 310$ µs in Fig. 20, the flame appears to be experiencing a DDT. For $310 \lesssim t - t_0 \lesssim 1080$ µs, the front speed oscillates between $0.7\widetilde{D_{CJ}}$ and $\widetilde{D_{CJ}}$, as would typically be expected of a quasi-detonation.

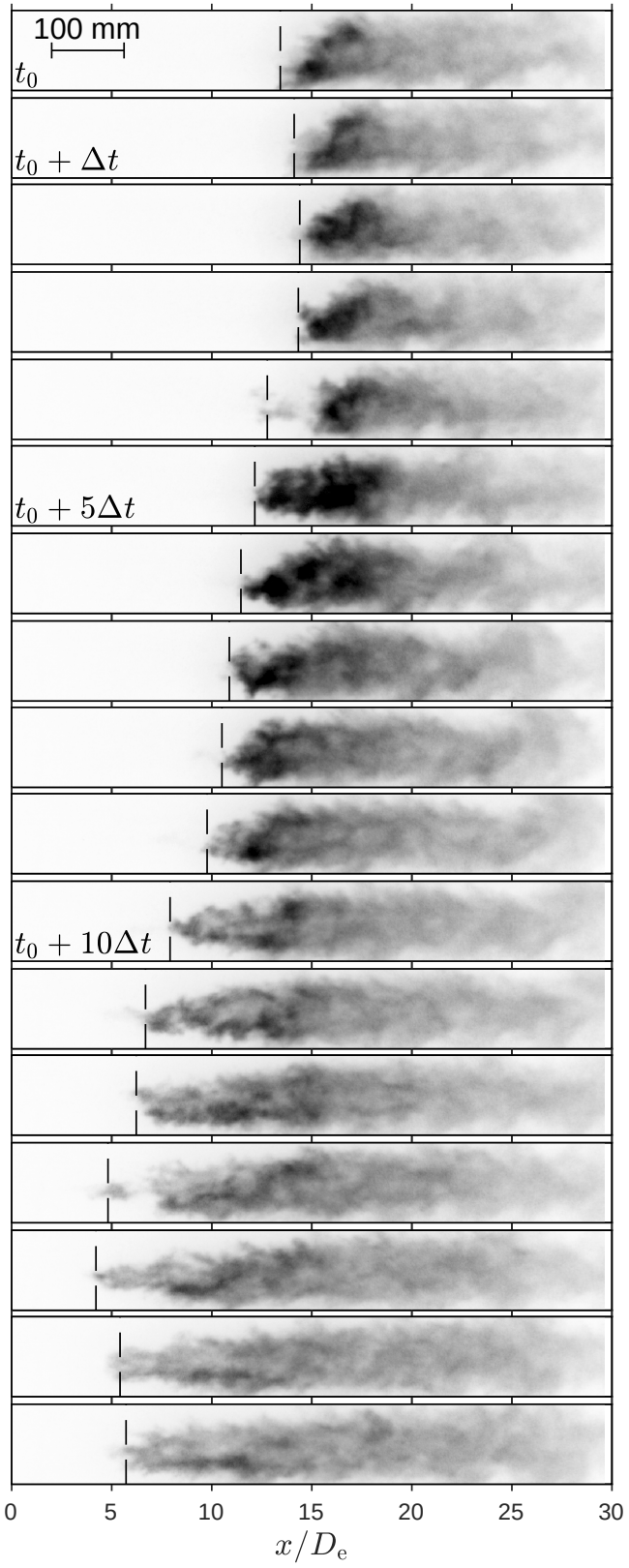

FIG. 19. Selection of OH* chemiluminescence snapshots showing a possible detonation propagation of the flame's leading-edge. The time interval between frames is $\Delta t \approx 77$ µs. The exposure (intensifier gate-time) is 20 µs.

Because the front speed is now larger than the local flow velocity, the front progresses upstream. For $t \gtrsim 1080$ µs, this regime fails and the flame velocity falls toward the choked deflagration regime. Consequently, the front progresses downstream since $s_\mathrm{f} < \widetilde{u_x}$.

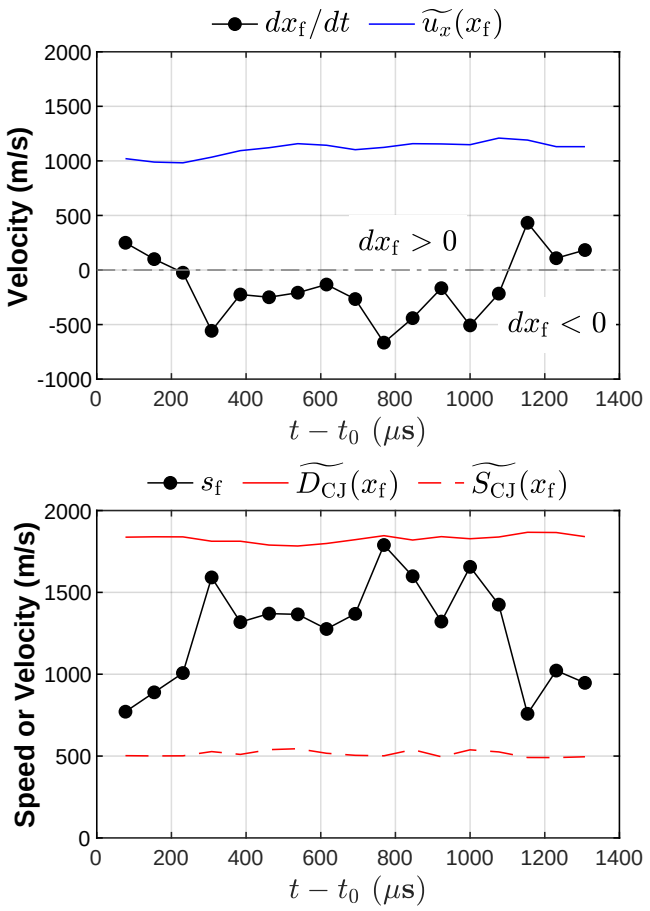

FIG. 20. Evolution of the displacement velocity dx_f/dt (top) and front speed s_f (bottom) corresponding to the sequence of Fig. 19.

Eventually, no combustion front could supersede the ideal CJ detonation, that is $s_\mathrm{f} \leq \widetilde{D_\mathrm{CJ}}$, except overdriven detonations. Consequently, when $s_\mathrm{f} \gg \widetilde{D_\mathrm{CJ}}$, the apparent leading edge propagation is actually resulting from the spontaneous ignition, *i.e.*, autoignition, of a new flame kernel such as in the sequence shown in Fig. 21. For this event, the velocity budget evolution is represented in Figure 22. For $t - t_0 < 460$ µs, which corresponds to the first seven frames of Fig. 21, the flame propagates with a near-constant speed very close to $\widetilde{S_\mathrm{CJ}}$. For $540 \lesssim t - t_0 \lesssim 615$ µs (between the eighth and ninth frames of Fig. 21), we clearly see the spontaneous creation of a new combustion kernel at about $x/D_\mathrm{e} = 6.8$.

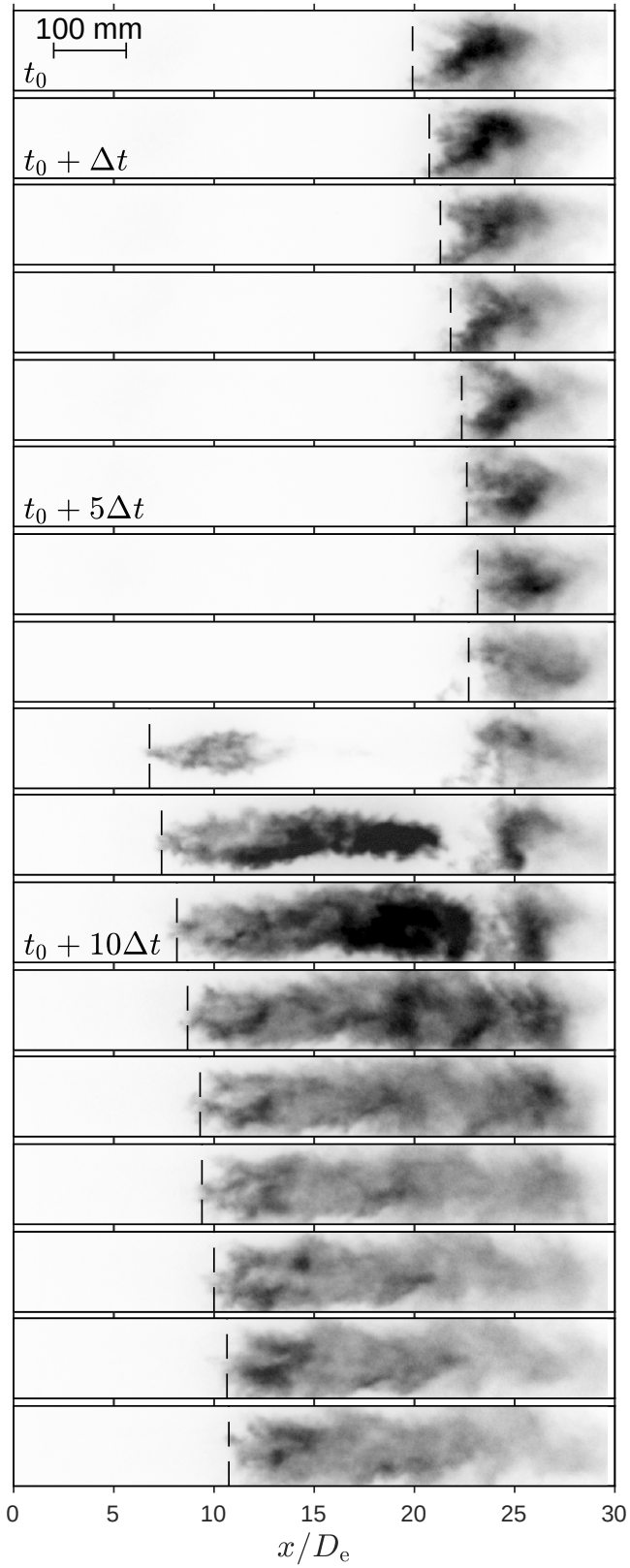

FIG. 21. Selection of OH* chemiluminescence snapshots showing the spontaneous creation of a new autoignition kernel at an extreme distance from the previous one. The time interval between frames is $\Delta t \approx 77$ µs. The exposure (intensifier gate-time) is 20 µs.

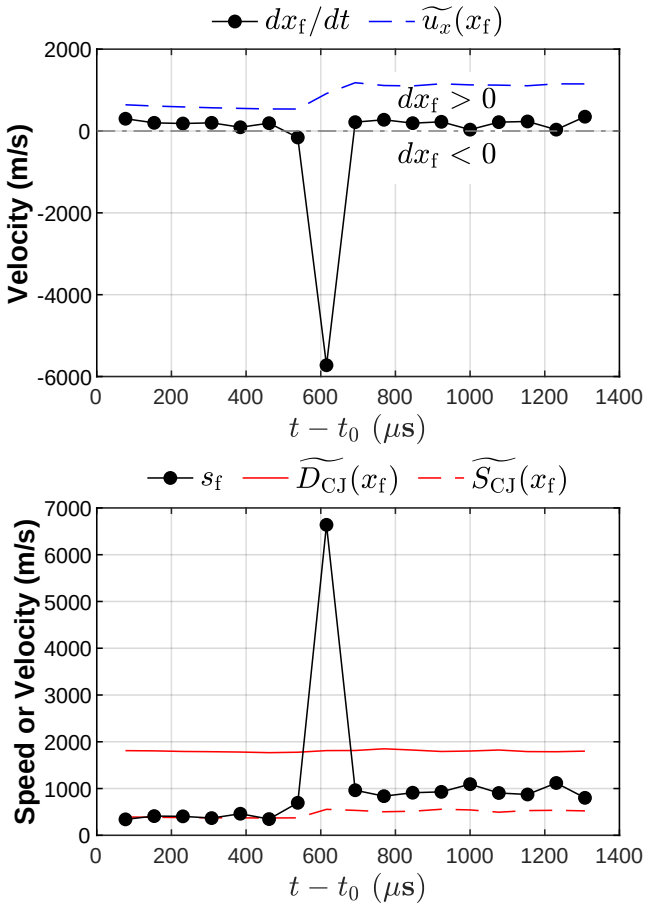

FIG. 22. Evolution of the displacement velocity dx_f/dt (top) and front speed s_f (bottom) corresponding to the sequence of Fig. 21.

The corresponding front speed would be about 7000 m/s, a magnitude, which could not realistically be attributed to any combustion front since this speed is much higher than $\widetilde{D_{CJ}}$. The autoignition prompts here because *(i)* too large a volume of unburnt gases has been left unconsumed between the nozzle exit and the previous front location, *(ii)* the still quite large temperature of the reacting mixture in the mixing layer and *(iii)* the proximity – at $x/D_e \approx 6.6$, *i.e.*, about 6 mm upstream – of a reflected shock intercepting the shear layer (see Fig. 12). Consequently, the volume of unreacted gases rapidly burns on the following frame. In fact, we notice that between the ninth and tenth frames, the trailing edge of the autoignition pocket progresses from $x/D_e \approx 13.9$ toward $x/D_e \approx 21.4$ corresponding to a displacement speed $dx_f/dt \approx 2700$ m/s. Since the normal vector to the front is here $\mathbf{n} = +\mathbf{e}_x$, we deduce that the combustion front propagates with a speed, $s_f = dx_f/dt - u_x \approx 1910$ m/s $\approx \widetilde{D_{CJ}}$, which suggests that the volume of unreacted gases is consumed by a detonation which rapidly transitioned from the autoignition kernel. As for the leading edge, its front seems to stabilize in the choked deflagration regime for the rest of the sequence. This constitutes a case of non-yet-realized DDT. The initial deflagration front progressively quenches after the emergence of the autoignition kernel since it is no longer fed with reactants.

VI. DISCUSSION

A. Unconfined DDT

The unsteady motion of the flame front, whether it be that of a detonation, a deflagration, a flashback, or an autoignition front, has been discussed in numerous scramjet combustor experiments, *e.g.*,[33–36]. To some extent, these constitute analog configurations to the one at hand, in as much as they relate to the combustion dynamics of a partially premixed supersonic flow. They, however, differ from our experiment in that the flame unsteady dynamics is found to be periodical with strong frequency peaks, whereas it is not the case here (see Fig. 9). Ishii *et al.*[37] have demonstrated the propagation of a CJ detonation in a supersonic premixed mixture flowing within a channel. However, to the best of our knowledge, detonation waves have never been experimentally demonstrated in freely propagating, *i.e.*, unconfined, non-premixed supersonic flows. Their existence is suggested in the numerical work of Bouheraoua *et al.*[3]. The dynamics illustrated in Figs. 19 and 20 may relate to the predictions suggested in[3] and consists of a combustion front, which seems to oscillate around the CJ detonation regime but fails to permanently do so since the CJ detonation velocity being larger than the flow velocity, the front is drawn upstream. The backward propagation of the detonation fails somewhere around $x/D_e = 4$, presumably because the mixture is here not enough premixed to sustain the detonation regime. The resulting (decoupled) deflagration is then pushed downstream until a new cycle begins.

Poludnenko *et al.*[29,38] numerically showed that high-intensity turbulence, albeit unconfined, can lead to a so-called *turbulence-induced spontaneous DDT*, whereby the transition to detonation is obtained without any assistance from the confining effect of walls or obstacles in characteristic length and time much shorter than those required for the *regular DDT* observed in quiescent confined media. Given the relatively high turbulence intensity of the jet – the jet Reynolds number is $\mathrm{Re} = 2.3 \times 10^5$ – this mechanism could well be responsible for the repeated initiation of detonations. To substantiate this point, let us examine how the combustion regime of the deflagration fronts compares to that of the DNS performed in [29,38], which exhibited turbulence-induced spontaneous DDT. To do so, we restrict ourselves to the positions where DDT is suspected to occur in the present investigation, *i.e.*, for $4 \lesssim x/D_e \lesssim 15$ according to Fig. 18. The classification of turbulent premixed combustion originally proposed by Borghi[39] allows the determination of the combustion regime based on the evaluation of two dimensionless groups, which express the competition between combustion and turbulence. These are the quantities: *(i)* ℓ_t/δ_ℓ^0 – where ℓ_t is the integral length scale and δ_ℓ^0 the flame thickness – and *(ii)* u'/s_L – where u' is the amplitude of the turbulent velocity fluctuations and s_L is the laminar flame speed. Their ratio defines a Damköhler number: $\mathrm{Da} = (\ell_t/\delta_\ell^0)/(u'/s_L)$, which we assimilate to the one used so far (see Eq. (1)). The laminar flame speed and flame thickness are linked to each other by $\delta_\ell^0 = \mathscr{D}/s_L$, where $\mathscr{D}$ is the mass diffusivity, which we assume

to be equal to the kinematic viscosity ν in the limit of a unity Schmidt number. It follows that the the turbulent Reynolds number writes $\mathrm{Re_t} = u'\ell_\mathrm{t}/\nu = (u'/s_\mathrm{L}) \times (\ell_\mathrm{t}/\delta^0_\ell)$, which we re-arrange into $u'/s_\mathrm{L} = \sqrt{\mathrm{Re_t}/\mathrm{Da}}$ and $\ell_\mathrm{t}/\delta^0_\ell = \sqrt{\mathrm{Re_t}\mathrm{Da}}$. For reference, the Karlovitz number is $\mathrm{Ka} = \sqrt{\mathrm{Re_t}}/\mathrm{Da}$. The turbulent Reynolds number $\mathrm{Re_t}$ is evaluated from the estimation of u' and ℓ_t sampled on the non-reactive RANS solution and weight-averaged according to Eq. (5). Any two of these three non-dimensional numbers allow for the evaluation of the combustion regime, as shown in the Borghi Diagram of Figure 23. For the most part, the deflagration front

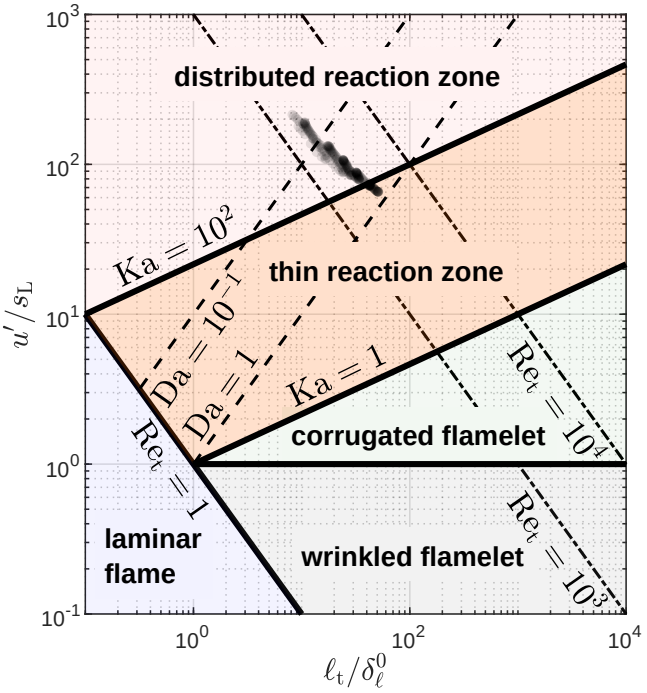

FIG. 23. Regimes of premixed turbulent combustion located (markers) in the Borghi diagram under conditions where DDT is suspected, *i.e.*, for $4 \lesssim x/D_\mathrm{e} \lesssim 15$ (see Fig. 18). The distributed reaction zone regime ($\mathrm{Ka} > 100$) corresponds to the regime where Poludnenko *et al.*[29,38] reported turbulence-induced spontaneous DDT.

is alleged to occur in the *distributed reaction zone* regime ($\mathrm{Ka} > 100$), which is characterized by a broad flame brush and no clear flame surface[40]. On the one hand, this explains the elongated aspect of the OH* chemiluminescence signal observed behind the front. On the other hand, this supports the mechanism of turbulence-induced spontaneous DDT, in as much as Poludnenko *et al.*[29,38] reported that spontaneous DDT was obtained for this regime. In fact, our observations could serve as evidence of such a mechanism in an actual unconfined medium, *i.e.*, contrary to the experiments[27] carried out with the presence of a tube confinement.

Upon examining the axial profile of the Karlovitz number shown in Figure 24, we notice that the $\mathrm{Ka} > 100$-criterion for the turbulence-induced DDT, is satisfied for $x/D_\mathrm{e} \lesssim 13$, which is in-line with the region where the detonation is presumably observed according to Fig. 18. Yet, we also note that the criterion is satisfied for $x/D_\mathrm{e} \gtrsim 25$, which is not consistent with the fact that we did not observe traces of detonation propagation, hence of DDT, there. We take this to the result from the fact that any time a deflagration is pushed so far downstream – because it has failed to transition – a new autoignition kernel is more likely to emerge upstream, as observed in Fig. 21, than for this deflagration to transition.

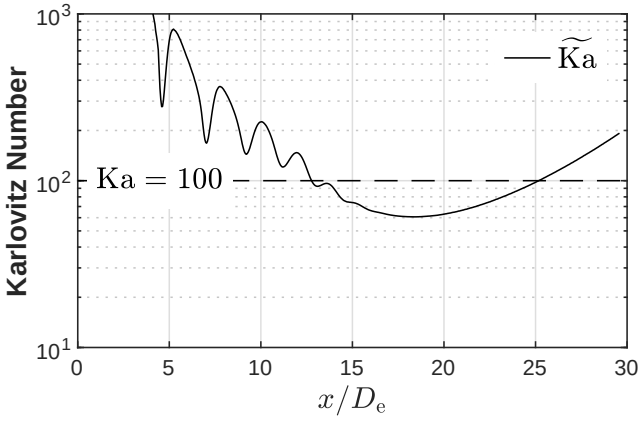

FIG. 24. Profile of $\widetilde{\mathrm{Ka}}$ along which the flame front allegedly propagates.

The presence of stationary shock waves (owing to the flow overexpansion) at regularly spaced intervals along the path of propagation certainly contributes, to second order, to achieving the critical conditions for the initiation of detonations. Such initiation is usually observed following the spontaneous formation of a hot spot, *i.e.*, an autoignition front, resulting from the reflection of transverse shocks at a solid wall or between themselves[32]. These transverse shocks or walls are not present here. Nonetheless, upon examining Fig. 18, we note that the region where detonations are presumably observed well corresponds to that where we noticed shock-induced Damköhler surges in the profile of Fig. 15. Conversely, the fact that the front speed never approaches the CJ detonation velocities for $x/D_\mathrm{e} \gtrsim 15$ is consistent with the evanescence of the shock cell structure downstream of $x/D_\mathrm{e} \approx 15$ (see for example the RANS temperature field in Fig. 12). Since it is presumed that DDT is promoted by the presence of these shocks, conversely, transition and acceleration are less likely to occur in this region.

Qualitatively, the mechanism for the repeated initiation of detonations could originate from a form of turbulence-induced spontaneous DDT assisted by the stationary shock cell structure. Finally, the relatively high temperature of the flow, about 800-1000 K, should in all likelihood be another promoter of DDT.

B. On the unsteadiness of the afterburning

The afterburning dynamics could be seen as locked to a self-perpetuating cycle, which hinders the flame from stabilizing. On the one hand, a steady-propagating deflagration – if we admit the conditions allowing for the establishment of the detonation regime are met – is in itself unstable, because it

is attracted toward the detonation regime through DDT, even more so because of the high turbulence intensity, the presence of the stationary shock cell structure and the overall high temperature of the flow. On the other hand, the local CJ detonation velocity is everywhere larger than the flow velocity. Therefore, a detonation front is also unstable since it will inevitably progress toward the upstream direction, where it will ultimately degenerate into a deflagration because the non-premixedness of the unburnt gases increases as the front approaches the nozzle exit. For the same reason, the transition of an accelerating deflagration front is not guaranteed and the probability of its occurrence should decrease with the level of non-premixedness. In either case, the deflagration front (whether decoupled or failed-to-transition) will be pushed downstream. It will keep on being pushed downstream for as long as the onset of a detonation does not occur or a new autoignition kernel emerges upstream.

Although the proposed mechanism provides a satisfactory explanation for the unsteady dynamics, further evidence is still required to support the alleged occurrence of the turbulence-induced DDT and the detonation propagation, as the available evidence is only circumstantial. Investigating the presence of non-stationary shock waves should be a crucial first step toward finding a conclusive evidence.

VII. STOCHASTIC MODEL FOR THE FRONT DYNAMICS

In order to validate the proposed description according to which the large-scale fluctuation of the afterburning is related to a self-perpetuating dynamic (see §VI B), we propose a stochastic description of the front propagation.

A. Markov chain modeling

Let us first consider a detonation front placed at position x. Its velocity relative to the flow is taken as the local detonation speed $\widetilde{D_{\mathrm{CJ}}}$, which is evaluated based on the local state of the non-reactive RANS solution. Hence, it moves with a velocity $\widetilde{u_x} - \widetilde{D_{\mathrm{CJ}}} < 0$ in the reference frame of the laboratory, *i.e.*, toward the nozzle.

Let us then postulate that the detonation failure mechanism involves a local failure rate $\dot{\omega}_Q$, which depends on the local Damköhler number and is essentially identical to the one employed in the field of reliability engineering. The accumulated probability of failing into a deflagration over a period of time Δt is thus $1-\exp(-\dot{\omega}_Q \Delta t)$. The front then propagates with absolute velocity $\widetilde{u_x} - \widetilde{S_{\mathrm{CJ}}}$, which is positive more often than not, *i.e.*, it moves away from the nozzle. A similar probabilistic process can be introduced for the front to transition back to a detonation front (DDT), with the associated transition rate $\dot{\omega}_P$.

This process corresponds to a local time-inhomogeneous Markov chain composed of two states, namely a *detonation state* (labeled DET) and a *deflagration state* (labeled DEF), as sketched in Figure 25. The probability that a deflagration transitions to a detonation (DEF $\rightarrow$ DET) is $P = 1-\exp(-\dot{\omega}_P \Delta t)$. The probability of not transitioning, *i.e.*, that the flame front persists as a deflagration (DEF $\rightarrow$ DEF) is $1-P$. Conversely, the probability of detonation failure (DET $\rightarrow$ DEF) is $Q = 1-\exp(-\dot{\omega}_Q \Delta t)$, and the probability that the detonation persists (DET $\rightarrow$ DET) is $1-Q$.

The transition and failure rates $\dot{\omega}_P$ and $\dot{\omega}_Q$ are modeled in such a way as to intuitively reproduce the observed phenomenology: the higher the local Damköhler, the more likely a deflagration will transition or a detonation will persist. Conversely, the smaller the Damköhler, the more likely a detonation will fail or a deflagration will miss the DDT. As a first approach, we choose the following formulations: $\dot{\omega}_P = \alpha \mathrm{Da}$ and $\dot{\omega}_Q = \beta/\mathrm{Da}$.

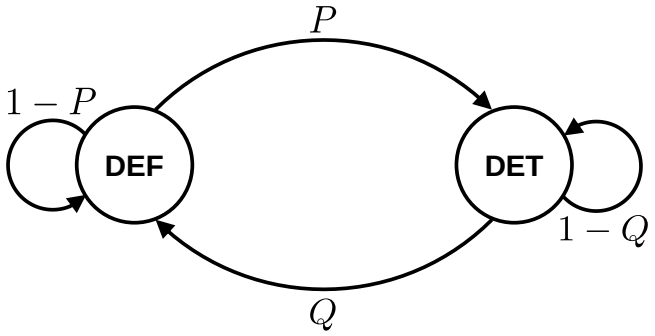

FIG. 25. Symbolic diagram of the proposed Markov chain model for the local transition and failure of the deflagration and detonation fronts.

B. Monte Carlo approach

For given values of α and β, a Monte Carlo simulation of the front dynamics can be performed. One chooses a random initial position and nature of the front and then lets it evolve over multiple time steps of duration Δt. At each step, we perform one iteration of the local Markov chain, possibly producing a state change. The front then moves with the adequate velocity for Δt. If the front happens to move out of the zone of interest, we reinitialize it at a random state (DEF or DET) and position, in an effort to mimic the autoignitions observed in our experiment. Suppose that the process is ergodic, the probability density distribution f_{eul} of the front position can be obtained by letting a single front evolve for a sufficiently long period. Statistical convergence may be accelerated by simulating the propagation of multiple independent fronts, *e.g.*, 10^3, over a shorter time frame.

C. Eulerian approach

The previous Monte Carlo approach, although simple and easy to implement, is, however, costly to converge with accuracy. Indeed, reaching a 1% relative error on f requires around 10^6 iterations for 10^3 tracked fronts, typically a few minutes of

computation on a single CPU-core. Monte Carlo approaches are known to converge in $1/\sqrt{n}$ with n the number of draws, hence reaching a better convergence rapidly becomes costly. Since we are willing to optimize the value of α and β to maximize the accuracy of our model, we aim at employing conventional optimization algorithms, which may need to iterate many times on the Monte Carlo process (for derivative-free approaches) and/or evaluate partial derivatives of f with respect to α and β (for derivative-based approaches), thus requiring a high accuracy on the convergence of f to avoid numerical noise. Therefore, in this section, we propose a more efficient and original approach to obtain the converged statistical distributions of the flame front position. It is based on the derivation of a continuous space-time model for the evolution of the density distributions of detonation and deflagration fronts. This model constitutes the Eulerian counterpart of the previous Lagrangian stochastic model.

Inspired by the previous Monte Carlo approach with multiple fronts being tracked at once for faster statistical convergence, we make the following thought experiment. Consider a large number N of fronts, which propagate independently, $N = N_{\text{det}} + N_{\text{def}}$, with N_{det} and N_{def} the number of detonation and deflagration fronts, respectively. We can compute a local detonation (resp. deflagration) density ρ_{det} (resp. ρ_{def}) as the number of corresponding fronts inside the small 1D volume δV of infinitesimal length δx centered around x, divided by δx. The sum $\rho_{\text{det}} + \rho_{\text{def}}$ represents the local probability density f_{eul}, up to a scaling, which will be discussed later. We can now construct a partial differential equation on the spatio-temporal evolution of these densities by performing a flux balance on the same infinitesimal volume, as sketched in Figure 26.

The number of deflagration fronts in δV is $N_{\text{def}} = \int_{\delta V} \rho_{\text{def}} \, \mathrm{d}V \approx \rho_{\text{def}} \delta x$. Let us list the various contributors to the variation of N_{def} over an infinitesimal time δt. Assuming the deflagrations are uniformly distributed in the volume, their motion through the right face at $x_{\text{R}} = x + \delta x/2$ produce a variation:

$$\delta N_{\text{def}}^{\text{R}} = -\left[\rho_{\text{def}} \left(\widetilde{u_x} - \widetilde{S_{\text{CJ}}}\right)\right]_{x_{\text{R}}} \delta t \tag{7}$$

, which is mostly negative (see Fig. 16). Similarly, deflagration fronts entering through the left face, at $x_{\text{L}} = x - \delta x/2$, produce a variation:

$$\delta N_{\text{def}}^{\text{L}} = \left[\rho_{\text{def}} \left(\widetilde{u_x} - \widetilde{S_{\text{CJ}}}\right)\right]_{x_{\text{L}}} \delta t \tag{8}$$

At the same time, the local population of deflagration fronts is subject to the DDT process, which is characterized by the transition rate ordinary differential equation (ODE): $d_t \rho_{\text{def}} = -\rho_{\text{def}} \dot{\omega}_P$. Hence, a negative variation $\delta N_{\text{def}}^{\ominus} = -\rho_{\text{def}} \dot{\omega}_P \delta x \delta t$ occurs over δt. Additionally, new deflagration fronts are generated locally by the failure of detonations, as dictated by the failure rate ODE: $d_t \rho_{\text{def}} = \rho_{\text{det}} \dot{\omega}_Q$, producing a positive variation $\delta N_{\text{def}}^{\oplus} = \rho_{\text{det}} \dot{\omega}_Q \delta x \delta t$.

Summing the various contributors to δN_{def}, we obtain :

$$\begin{aligned} \delta N_{\text{def}} &= \delta N_{\text{def}}^{\text{R}} + \delta N_{\text{def}}^{\text{L}} + \delta N_{\text{def}}^{\oplus} + \delta N_{\text{def}}^{\ominus} \\ &= \delta t \left[\rho_{\text{def}} (\widetilde{u_x} - \widetilde{S_{\text{CJ}}})\right]_{x_{\text{R}}}^{x_{\text{L}}} + \delta x \delta t (\rho_{\text{det}} \dot{\omega}_Q - \rho_{\text{def}} \dot{\omega}_P) \end{aligned} \tag{9}$$

Using the relation $\delta \rho_{\text{def}} \delta x = \delta N_{\text{def}}$ and dividing by δx, we get:

$$\frac{\delta \rho_{\text{def}}}{\delta t} = \frac{1}{\delta x} \left[\rho_{\text{def}} (\widetilde{u_x} - \widetilde{S_{\text{CJ}}})\right]_{x_{\text{R}}}^{x_{\text{L}}} + (\rho_{\text{det}} \dot{\omega}_Q - \rho_{\text{def}} \dot{\omega}_P) \tag{10}$$

An identical analysis can be performed for the local density ρ_{det} of detonation fronts. We then let δx and δt tend to 0 to obtain partial derivatives, yielding the following system of partial differential equations:

$$\partial_t \begin{pmatrix} \rho_{\text{det}} \\ \rho_{\text{def}} \end{pmatrix} + \partial_x \begin{pmatrix} (\widetilde{u_x} - \widetilde{D_{\text{CJ}}}) \rho_{\text{det}} \\ (\widetilde{u_x} - \widetilde{S_{\text{CJ}}}) \rho_{\text{def}} \end{pmatrix} = \begin{pmatrix} -\dot{\omega}_Q & \dot{\omega}_P \\ \dot{\omega}_Q & -\dot{\omega}_P \end{pmatrix} \begin{pmatrix} \rho_{\text{det}} \\ \rho_{\text{def}} \end{pmatrix} \tag{11}$$

Boundary conditions must be prescribed at the left and right boundaries. Mimicking the previous Monte Carlo approach, we redistribute uniformly in space the fluxes of detonation and deflagration fronts lost at the boundaries. In the case where a component of the convective flux at a boundary is oriented toward the inside of the computational domain, we force it to 0, since we assume that no fronts enter from the outside, in coherence with our previous stochastic approach. Note that the model is linear in densities, *i.e.*, their absolute values do not matter, only their value relative to each other. This simple convective-reactive system can be discretized in space using a cell-centered finite-volume method on n cells with, *e.g.*, a first-order upwind scheme, yielding a system of ordinary differential equations $X' = F(X)$, with $X = (\rho_{\text{det}}^1, \rho_{\text{def}}^1, \ldots, \rho_{\text{det}}^n, \rho_{\text{def}}^n)^t$ and F the discrete space operator.

We are interested in the stationary profiles $\rho_{\text{det}}(x)$ and $\rho_{\text{def}}(x)$. Thus, starting from a non-trivial initial condition X_0, *e.g.*, non-zero uniform fields, we can march our system forward in time until it reaches its steady-state solution X^*. Alternatively, we can directly search for the root of F using Newton's method. In our case, using linear space schemes for the convection term leads to F being linear. Hence, we can directly solve for $F(X^*) = (\partial_x F) X^* = 0$. However, this linearity implies that any multiple of X^* is also a solution, *i.e.*, the steady-state system is ill-posed. To remedy this issue, we choose one cell (index i) where we replace the balance equation of ρ_{det}^i by the algebraic equation $\rho_{\text{det}}^i = 1$. This Dirichlet condition ensures the well-posedness of the problem. We then scale the solution so that $\int_x f_{\text{eul}} \, \mathrm{d}x = \int_x (\rho_{\text{det}} + \rho_{\text{def}}) \, \mathrm{d}x = 1$, *i.e.*, f_{eul} corresponds to a probability density function. A well-resolved result (on 10^3 cells) is typically obtained in less than a second on a single CPU-core.

D. Optimization and results

Via a classical gradient-based optimization method, an optimal solution is obtained for the coefficients, which mini-

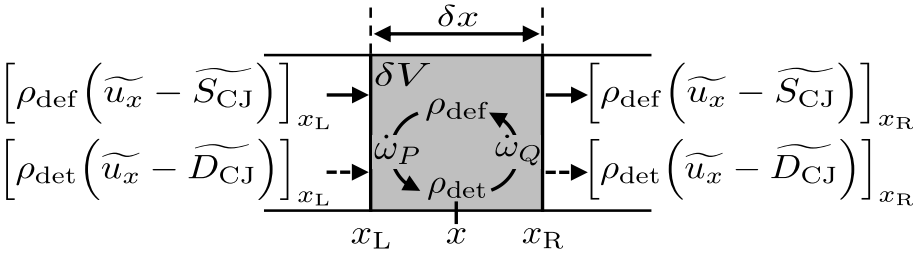

FIG. 26. Sketch of the flux balance on the infinitesimal volume δV. The fluxes at $x_{\rm R}$ need to be accounted for negatively since they are outbound.

mizes the error between the simulated probability density distribution f and that of the experiment: $\alpha = 8836$ s^{-1} and $\beta = 662$s^{-1}. The probability density distribution obtained with these parameters is plotted in Figure 27. We see that $f_{\rm eul}$, computed with 4×10^3 cells, and $f_{\rm mc}$, computed with 10^3 fronts, 7×10^4 time steps and $\Delta t = 10^{-6}$ s, are in close agreement, the difference being within the convergence accuracy of the Monte Carlo procedure. The numerical and experimental distributions are found close to each other. This is quite remarkable considering the simplifying assumptions, in particular, *(i)* that of the premixed nature of the reactive mixture, *(ii)* the one-dimensional front propagation, *(iii)* the step changes of the velocity between $\widetilde{S_{\rm CJ}}$ and $\widetilde{D_{\rm CJ}}$, which imply infinite acceleration or deceleration, and *(iv)* the simple forms of the probability laws.

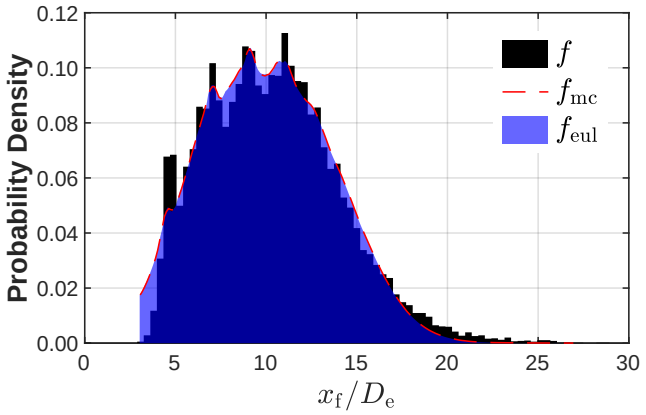

FIG. 27. Comparison of the probability density distributions of the flame's leading edge axial position obtained from the OH* chemiluminescence recording (f) to those obtained using the Markov-chain model combined with a Monte Carlo approach ($f_{\rm mc}$) and the Eulerian approach ($f_{\rm eul}$).

The optimized parameters α and β of the model are not universal but depend on the definition of the Damköhler, in particular the weight-averaging operation and the chemical kinetic scheme. Instead of providing absolute physical constants, the purpose of the model is rather to prove our phenomenological interpretation translated into the form of a simple model can reproduce the complex unsteady dynamics of the experiment.

VIII. CONCLUSIONS

In this work, we have discussed the complex dynamics of the unstable afterburning developing in a fuel-rich supersonic overexpanded plume exhausting from a model rocket engine. The analysis of the afterburning – recorded by means of OH* chemiluminescence high-speed imaging – reveals large-scale stochastic variations of the flame's leading edge position, with amplitude of variation spanning about 25 nozzle diameters in the axial direction.

As opposed to the classical case study reported by Cheng *et al.*[2], which has been widely considered as a validation case of CFD-based approaches for supersonic combustion applications, the proposed case study may well be even more challenging to reproduce, owing to the large-scale combustion unsteadiness. From a phenomenological viewpoint, the afterburning lack of stability could be linked to the fact that the jet exhaust velocity lies close to the blowout velocity, of the considered fuel blend. To prove this point, we could experiment with an exhaust velocity larger or lower.

On a general note, steady combustion could be – and may have been more often than not – misinterpreted if observed at too-low the acquisition rate. The described phenomenon, which was obtained through serendipity, would have been easily missed if not for the high-speed imaging setup.

The analysis of the flame's leading edge dynamics allows to determine that the propagation speed of its front (relative to the flow) is compatible with Chapman-Jouguet detonation or deflagration velocities, although, on rare occasions, autoignition occurs, presumably because too large a volume of fresh gases has been left unconsumed, following excessive downstream propagation of the front. The afterburning behaves somehow as a self-perpetuating dynamic system unable to stabilize because of the following considerations. A deflagration front is attracted toward the detonation regime possibly owing to the high turbulence intensity of the flow. The mechanism of DDT could link to the turbulence-induced spontaneous DDT suggested by Poludnenko *et al.*[29] assisted by the stationary shock cell structure at regularly spaced interval resulting from the flow overexpansion, and an overall hot temperature of the flow. Detonation velocities for the local compositions sampled along the most reactive streamline are everywhere larger than the flow velocity. As such, a formed detonation is doomed to propagate upstream, where it ultimately fails when the composition is no longer compatible with this

regime. It then degenerates into a slower deflagration front of a velocity lower than that of the local flow. Thus, the front is pushed downstream. In some occasions, the front is pushed too far downstream – if it fails to achieve DDT – which in turn leads to the growth of a relatively large cloud of unreacted gases within which a new autoignition kernel emerges, and a new cycle begins. The cycle is however aperiodic and consists of stochastic time-varying phases. Stochasticity is a common trait of DDT and autoignition phenomena, so it should not be surprising to observe it here. Besides, the fluctuations could also originate from the turbulence-based non-uniformity of the flow and composition exhausting from the nozzle.

Our observations may well confirm the existence of turbulence-induced DDT and unsteady detonation-wave propagation in unconfined counter-flowing supersonic flow, a phenomenon, which has been conjectured theoretically or suggested numerically but, to the best of our knowledge, has never been observed experimentally. Further works are still needed to confirm our interpretation. The use of Schlieren visualization, with an ultra-fast camera setup to capture the propagation of the front, should help in precising the nature of the flame front propagation. Traces of non-stationary shock waves should provide a solid evidence to support the intermittent presence of detonations. Besides, the possible azimuthal and/or radial motions of the front could be tracked using a second synchronized OH* chemiluminescence setup positioned in such a way as to visualize the jet exhaust from the rear.

Finally, we derived a phenomenological stochastic model, which is able to reproduce the probability density distribution of the flame's leading edge axial position. This model well supports our interpretation according to which the afterburning consists of a self-perpetuating unstable dynamics.

ACKNOWLEDGMENTS

This work was funded by ONERA, the French Aerospace Lab. We gratefully acknowledge the contributions of François Vuillot and Yves Mauriot for managing the experimental campaign, of Nicolas Fdida for the support in setting up the visualization apparatus, and of Aurélie Covasso and Éric Paux for the preparation and conduct of the experiment. The authors thank Aurélie Nicole for initiating the RANS computation. We thank Antoine Simon for supporting the analyses.

AUTHOR DECLARATIONS

Conflict of Interest

The authors have no conflicts to disclose.

Author Contributions

Stéphane Boulal: conceptualization (lead); data curation (lead); formal analysis (lead); investigation (equal); methodology (lead); visualization (lead); writing – original draft (lead); writing – review and editing (lead). **Adrien Langenais**: data curation (equal); formal analysis (equal); visualization (equal); writing – original draft (equal); writing – review and editing (equal). **Laurent François**: formal analysis (equal); methodology (equal); writing – original draft (equal); writing – review and editing (equal). **Pierre Bernigaud**: methodology (equal); writing – review and editing (equal). **Lucien Vingert**: investigation (equal); project administration (lead); resources (lead); writing – review and editing (equal).

DATA AVAILABILITY

The data that support the findings of this study are available from the corresponding author upon reasonable request.

[1]D. Scherrer, O. Dessornes, M. Ferrier, A. Vincent-Randonnier, Y. Moule, and V. Sabel'nikov, "Research on Supersonic Combustion and Scramjet Combustors at ONERA," AerospaceLab J. **11** (2016).
[2]T. S. Cheng, J. A. Wehrmeyer, R. W. Pitz, O. Jarrett, and G. B. Northam, "Raman measurement of mixing and finite-rate chemistry in a supersonic hydrogen-air diffusion flame," Combust. Flame **99**, 157–173 (1994).
[3]L. Bouheraoua, P. Domingo, and G. Ribert, "Large-eddy simulation of a supersonic lifted jet flame: Analysis of the turbulent flame base," Combust. Flame **179**, 199–218 (2017).
[4]T. C. Lieuwen, Unsteady combustor physics (Cambridge University Press, Cambridge, U.K., 2021).
[5]S. Boulal, A. Genot, J.-M. Klein, Y. Fabignon, A. Vincent-Randonnier, and V. Sabelnikov, "On the hydro-acoustic coupling responsible for the flashback limit-cycle of a premixed flame at a backward-facing step," Combust. Flame **257**, 112999 (2023).
[6]W. H. Calhoon, "Computational Assessment of Afterburning Cessation Mechanisms in Fuel-Rich Rocket Exhaust Plumes," J. Prop. Power **17**, 111–119 (2001).
[7]D. Gueyffier, B. Fromentin-Denoziere, J. Simon, A. Merlen, and V. Giovangigli, "Numerical Simulation of Ionized Rocket Plumes," J. Thermophys. Heat Transfer **28**, 218–225 (2014).
[8]A. Langenais, J. Aubrée, P. Doublet, S. Langlois, and V. Rialland, "Numerical simulation of flight effect on the afterburning plume exhausting from a solid rocket motor," Proceedings of the 10th European Conference for Aeronautics and Space Sciences (EUCASS) (2023).
[9]A. D. Birch and G. K. Hargrave, "Lift-off heights in underexpanded natural gas jet flames," Symp. (Int.) Combust. **22**, 825–831 (1989).
[10]J. A. Hammer and A. Roshko, "Temporal Behavior of Lifted Turbulent Jet Flames," Combust. Sci. Technol. **155**, 75–103 (2000).
[11]A. Cessou, C. Maurey, and D. Stepowski, "Parametric and statistical investigation of the behavior of a lifted flame over a turbulent free-jet structure," Combust. Flame **137**, 458–477 (2004).
[12]N. J. Moore and K. M. Lyons, "Leading-Edge Flame Fluctuations in Lifted Turbulent Flames," Combust. Sci. Technol. **182**, 777–793 (2010).
[13]S. Boulal, N. Fdida, L. Matuszewski, L. Vingert, and M. Martin-Benito, "Flame dynamics of a subscale rocket combustor operating with gaseous methane and gaseous, subcritical or transcritical oxygen," Combust. Flame **242**, 112179 (2022).
[14]A. Towne, O. T. Schmidt, and T. Colonius, "Spectral proper orthogonal decomposition and its relationship to dynamic mode decomposition and resolvent analysis," J. Fluid Mech. **847**, 821–867 (2018).
[15]Y. Moule, V. Sabelnikov, and A. Mura, "Highly resolved numerical simulation of combustion in supersonic hydrogen–air coflowing jets," Combust. Flame **161**, 2647–2668 (2014).
[16]Z. Huang, M. J. Cleary, Z. Ren, and H. Zhang, "Large eddy simulation of a supersonic lifted hydrogen flame with sparse-Lagrangian multiple mapping conditioning approach," Combust. Flame **238**, 111756 (2022).
[17]J. Troyes, I. Dubois, V. Borie, and A. Boischot, "Multi-phase reactive numerical simulations of a model solid rocket motor exhaust jet," 42nd

AIAA/ASME/SAE/ASEE Joint Propulsion Conference and Exhibit, Sacramento, CA, USA , , AIAA 2006–4414 (2006).
[18] D. Scherrer, F. Chedevergne, P. Grenard, J. Troyes, A. Murrone, E. Montreuil, F. Vuillot, N. Lupoglazoff, M. Huet, B. Sainte-Rose, N. Bertier, J.-M. Lamet, T. Le Pichon, E. Radenac, A. Nicole, L. Matuszewski, and M.-P. Errera, "Recent CEDRE applications," AerospaceLab J. **2**, AL02–13 (2011).
[19] A. Refloch, B. Courbet, A. Murrone, P. Villedieu, C. Laurent, P. Gilbank, J. Troyes, L. Tessé, G. Chaineray, J.-B. Dargaud, E. Quémerais, and F. Vuillot, "CEDRE software," AerospaceLab J. **2**, AL02–11 (2011).
[20] F. Menter, M. Kuntz, and R. Langtry, "Ten years of industrial experience with the SST turbulence model," Turb. Heat and Mass Transfer **4**, 625–632 (2003).
[21] F. Menter, "Improved two-equation k-omega turbulence models for aerodynamic flows," Technical Memorandum 103975 (NASA, 1992).
[22] S. Pope, "An explanation of the turbulent round-jet/plane-jet anomaly," AIAA J. **16**, 279–281 (1978).
[23] S. Sarkar, "The pressure-dilatation correlation in compressible flows," Phys. Fluids A **4**, 2674–2682 (1992).
[24] N. Peters, Turbulent combustion (Cambridge University Press, Cambridge, U.K., 2000).
[25] W. Breitung, C. Chan, S. Dorofeev, A. Eder, B. Gelfand, M. Heitsch, R. Klein, A. Malliakos, E. Shepherd, E. Studer, and P. Thibault, "Flame Acceleration and Deflagration-to-Detonation Transition in Nuclear Safety." State-of-the Art Report by a Group of Experts NEA/CSNI/R(2000)7 (Nuclear Energy Agency, 2000).
[26] G. Dupre, O. Peraldi, J. H. S. Lee, and R. Knystautas, "Propagation of detonation waves in an acoustic absorbing walled tube," Proc. Astronaut. Aeronaut **114**, 248–263 (1988).
[27] A. Y. Poludnenko, J. Chambers, K. Ahmed, V. N. Gamezo, and B. D. Taylor, "A unified mechanism for unconfined deflagration-to-detonation transition in terrestrial chemical systems and type Ia supernovae," Science **366**, eaau7365 (2019).
[28] R. Hytovick, C. Rising, A. Morales, T. Genova, J. Berson, and K. Ahmed, "The effects of flame generated turbulence for turbulent-induced deflagration to detonation transition," Proc. Combust. Inst. **39**, 2817–2824 (2023).
[29] A. Y. Poludnenko, T. A. Gardiner, and E. S. Oran, "Spontaneous transition of turbulent flames to detonations in unconfined media," Phys. Rev. Lett. **107** (2011).
[30] X. Lu, C. R. Kaplan, and E. S. Oran, "Predictions of flame acceleration, transition to detonation, and detonation propagation using the Chemical-Diffusive Model," Combust. Flame **235**, 111705 (2022).
[31] J. Lee, The Detonation Phenomenon (Cambridge University Press, 2008).
[32] S. Boulal, P. Vidal, R. Zitoun, T. Matsumoto, and A. Matsuo, "Experimental investigation on detonation dynamics through a reactivity sink," Combust. Flame **196** (2018).
[33] D. J. Micka and J. F. Driscoll, "Combustion characteristics of a dual-mode scramjet combustor with cavity flameholder," Proc. Combust. Inst. **32**, 2397–2404 (2009).
[34] M. L. Fotia and J. F. Driscoll, "Ram-Scram Transition and Flame/Shock-Train Interactions in a Model Scramjet Experiment," J. Prop. Power **29**, 261–273 (2013).
[35] M.-B. Sun, X.-D. Cui, H.-B. Wang, and V. Bychkov, "Flame flashback in a supersonic combustor fueled by ethylene with cavity flameholder," J. Propul. Power **31**, 976–981 (2015).
[36] Z.-G. Wang, M.-B. Sun, H.-B. Wang, J.-F. Yu, J.-H. Liang, and F.-C. Zhuang, "Mixing-related low frequency oscillation of combustion in an ethylene-fueled supersonic combustor," Proc. Combust. Inst. **35**, 2137–2144 (2015).
[37] K. Ishii, H. Kataoka, and T. Kojima, "Initiation and propagation of detonation waves in combustible high speed flows," Proc. Combust. Inst. **32**, 2323–2330 (2009).
[38] A. Y. Poludnenko, "Pulsating instability and self-acceleration of fast turbulent flames," Phys. Fluids **27**, 014106 (2015).
[39] R. Borghi, "On the structure and morphology of turbulent premixed flames," Recent advances in the Aerospace Sciences , 117–138 (1985).
[40] A. J. Aspden, M. S. Day, and J. B. Bell, "Turbulence–flame interactions in lean premixed hydrogen: transition to the distributed burning regime," J. Fluid Mech. **680**, 287–320 (2011).